A carbon sink-driven approach to estimate gross primary production from microwave satellite observations

Irene E. Teubner[a,*], Matthias Forkel[a], Gustau Camps-Valls[b], Martin Jung[c], Diego G. Miralles[d], Gianluca Tramontana[e], Robin van der Schalie[f], Mariette Vreugdenhil[a], Leander Mösinger[a], Wouter A. Dorigo[a]

[a]*Department of Geodesy and Geoinformation, TU Wien, Gußhausstraße 27-29, 1040 Vienna, Austria*
[b]*Image and Signal Processing Group (ISP), Universitat de València, Calle Catedrático José Beltrán 2, 46980 Paterna (València), Spain*
[c]*Department for Biogeochemical Integration, Max Planck Institute for Biogeochemistry, P.O. Box 10 01 64, 07701 Jena, Germany*
[d]*Laboratory of Hydrology and Water Management, Ghent University, Campus Coupure, Coupure links 653, B-9000 Ghent, Belgium*
[e]*Department for Innovation in Biological Agro-food and Forest systems (DIBAF), Tuscia University, Via San Camillo de Lellis s.n.c.- 01100 Viterbo, Italy*
[f]*VanderSat B.V., Wilhelminastraat 43a, 2011 VK, Haarlem, The Netherlands*

Abstract

Global estimation of Gross Primary Production (GPP) – the uptake of atmospheric carbon dioxide by plants through photosynthesis - is commonly based on optical satellite remote sensing data. This presents a source-driven

*Corresponding author
Email addresses: irene.teubner@gmx.at (Irene E. Teubner), matthias.forkel@geo.tuwien.ac.at (Matthias Forkel), gcamps@uv.es (Gustau Camps-Valls), mjung@bgc-jena.mpg.de (Martin Jung), diego.miralles@UGent.be (Diego G. Miralles), g.tramontana@unitus.it (Gianluca Tramontana), rvanderschalie@vandersat.com (Robin van der Schalie), Mariette.Vreugdenhil@geo.tuwien.ac.at (Mariette Vreugdenhil), leander.moesinger@geo.tuwien.ac.at (Leander Mösinger), Wouter.Dorigo@geo.tuwien.ac.at (Wouter A. Dorigo)

approach since it uses the amount of absorbed light, the main driver of photosynthesis, as a proxy for GPP. Vegetation Optical Depth (VOD) estimates obtained from microwave sensors provide an alternative and independent data source to estimate GPP on a global scale, which may complement existing GPP products. Recent studies have shown that VOD is related to aboveground biomass, and that both VOD and temporal changes in VOD relate to GPP. In this study, we build upon this concept and propose a model for estimating GPP from VOD. Since the model is driven by vegetation biomass, as observed through VOD, it presents a carbon sink-driven approach to quantify GPP and, therefore, is conceptually different from common source-driven approaches. The model developed in this study uses single frequencies from active or passive microwave VOD retrievals from C-, X- and Ku-band (Advanced Scatterometer (ASCAT) and Advanced Microwave Scanning Radiometer for Earth Observation (AMSR-E)) to estimate GPP at the global scale. We assessed the ability for temporal and spatial extrapolation of the model using global GPP from FLUXCOM and in situ GPP from FLUXNET. We further performed upscaling of in situ GPP based on different VOD data sets and compared these estimates with the FLUXCOM and MODerate-resolution Imaging Spectroradiometer (MODIS) GPP products. Our results show that the model developed for individual grid cells using VOD and change in VOD as input performs well in predicting temporal patterns in GPP for all VOD data sets. For spatial extrapolation of the model, however, additional input variables are needed to represent the spa-

tial variability of the VOD-GPP relationship due to differences in vegetation type. As additional input variable, we included the grid cell median VOD (as a proxy for vegetation cover), which increased the model performance during cross validation. Mean annual GPP obtained for AMSR-E X-band data tends to overestimate mean annual GPP for FLUXCOM and MODIS but shows comparable latitudinal patterns. Overall, our findings demonstrate the potential of VOD for estimating GPP. The sink-driven approach provides additional information about GPP independent of optical data, which may contribute to our knowledge about the carbon source-sink balance in different ecosystems.
Keywords: microwave remote sensing, vegetation optical depth, ecosystem productivity, ASCAT, AMSR-E, AMSR2

1. Introduction

The uptake of the greenhouse gas carbon dioxide by vegetation during photosynthesis, i.e. Gross Primary Production (GPP), is a key ecosystem process. Estimation of GPP from satellite observations commonly uses optical data together with empirical or semi-empirical models (Gilabert et al., 2017; Running et al., 2004) or machine learning approaches (Beer et al., 2010; Jung et al., 2011; Tramontana et al., 2016; Yang et al., 2007). Biophysical properties obtained from optical remote sensing that are often used to estimate GPP include the fraction of Absorbed Photosynthetically Active Radiation (fAPAR), Normalized Difference Vegetation Index (NDVI), or Leaf

Area Index (LAI). These approaches rely on the light-use efficiency theory (Monteith, 1972) whereby GPP depends on the incoming Photosynthetically Active Radiation (PAR), the fraction of PAR that is absorbed, i.e. fAPAR, and the efficiency of converting light to assimilated carbon (Beer et al., 2010; Gilabert et al., 2017; Jung et al., 2011; Running et al., 2004; Tramontana et al., 2016; Yang et al., 2007). Another variable retrieved from optical data is Solar-Induced chlorophyll Fluorescence (SIF), which is a measure for photosynthetic activity (Frankenberg et al., 2011; Guan et al., 2016). SIF has received much attention in recent years, because of its linear relationship with GPP at canopy scale (Damm et al., 2015; Frankenberg et al., 2014; Guanter et al., 2014; Zhang et al., 2016), especially at coarser temporal resolution like monthly sampling (Guanter et al., 2014). SIF has also been used for estimating GPP globally through the use of artificial neural networks (Alemohammad et al., 2017). Optical biophysical properties provide an estimate for the amount of carbon that is taken up by plants based on the absorption (fAPAR) or re-emission (SIF) of sunlight (source-driven). In recent years, however, it has been proposed that plant growth may be stronger limited by sink- rather than source-activity (Fatichi et al., 2014; Körner, 2015), and that considering sinks of fixed carbon can improve constrains in global vegetation models (Leuzinger et al., 2013).

Microwave Vegetation Optical Depth (VOD) is a measure of the attenuation of microwave radiation caused by vegetation (Woodhouse, 2005) and thus relates to the total vegetation water content (Jackson and Schmugge, 1991). VOD can be retrieved from different frequencies/wavelengths in the microwave region, which can provide information on different parts of the canopy. In theory, lower frequencies like L-band are more sensitive to large plant structures like stems and large branches, while higher frequencies like X-band are more closely related to small structures like leaves and twigs (Woodhouse, 2005). Microwave satellite observations at frequencies below 10 GHz are not affected by cloud cover (Woodhouse, 2005). Therefore, VOD can provide valuable information on the vegetation layer in addition to products derived from optical remote sensing data.

In recent years, studies have proposed to use VOD to estimate aboveground living biomass (Liu et al., 2011, 2015; Momen et al., 2017; Rodríguez-Fernández et al., 2018; Tian et al., 2016). Biomass and/or temporal change in biomass, however, relate to Net Primary Production (NPP) (Clark et al., 2001a,b; Girardin et al., 2010; Gower et al., 2001; Lavigne and Ryan, 1997; Luyssaert et al., 2007) and to Autotrophic Respiration (R_a) (Lavigne and Ryan, 1997; Ryan, 1990), the sum of which constitutes GPP (e.g. Bonan, 2015; Odum, 1959). Due to this causal relationship between biomass and GPP, a relationship is expected between VOD and GPP. Teubner et al. (2018) showed that both the original VOD time series (VOD) and the temporal change in VOD (ΔVOD) are correlated to GPP and suggested that the combination of VOD and ΔVOD has the potential to provide complementary information to GPP estimates from optical data.

In this study, we build upon the explorative work of Teubner et al. (2018)

and develop a model to estimate GPP based on VOD using Generalized Additive Models (GAM; Hastie and Tibshirani, 1987). Complementary to source-driven approaches, we are proposing a model that is driven by vegetation biomass, as expressed through VOD, which thus presents a sink-driven approach that does not depend on PAR as model input. We assessed the performance of VOD observations from different sensors and multiple frequencies, since it is not clear which frequencies most closely relate to GPP. As input variables to the model, we use different VOD variables, i.e. VOD, ΔVOD and the temporal grid cell median VOD ($mdnVOD$). The latter serves as a proxy for land cover and thus aids the spatial extrapolation of the model to different vegetation types without requiring further ancillary data. Due to the complex relationship between VOD and GPP, we conducted a separate analysis based on SIF using similar experimental setups as for VOD. This additional analysis gives insight into differences in model performance between setups that are not caused by using VOD variables as input to the model. The aim of this study is 1) to assess the model's capability for temporal extrapolation, 2) to evaluate the model's performance in spatial extrapolation and determine the required model structure using model selection, and 3) to perform upscaling of in situ FLUXNET GPP and compare the upscaled VOD-based GPP estimates with global GPP estimates from FLUXCOM and the MODerate-resolution Imaging Spectroradiometer (MODIS).

2. Data sets

The analysis is based on the period from 2007 to 2015 and uses VOD data from C-, X- and Ku -band and various GPP data sets. The data sets have different temporal coverage, which is summarized for VOD and GPP data in Table 1. Global temporal median maps of the remotely sensed VOD and GPP data sets are displayed in Fig. S1. For FLUXNET data, a list of the sites and graphs illustrating the location and data coverage are given in Table S1 and Fig. S2.

Our analysis was carried out for different passive VOD frequencies from both the Advanced Microwave Scanning Radiometer for Earth Observation System (AMSR-E) and its successor the Advanced Microwave Scanning Radiometer 2 (AMSR2). The overlap period between AMSR2 and in situ FLUXNET data, however, is considerably short (2 years and 5 months) and is further reduced by the lower number of FLUXNET sites in the later period, which potentially leads to less robust results in some parts of the analysis. For this reason and because AMSR-E and AMSR2 generally yielded similar results, the study focuses on results for AMSR-E. For results using AMSR2 frequencies, please see the supplement.

2.1. VOD data sets

2.1.1. ASCAT VOD

The Advanced Scatterometer (ASCAT) is an active microwave sensor measuring C-band (5.25 GHz) backscatter in vertical co-polarization and flies

Table 1: Data set overview for VOD and GPP data sets. Acronyms – EVI: Enhanced Vegetation Index, fAPAR: fraction of Absorbed Photosynthetically Active Radiation, LAI: Leaf Area Index, MIR: MODIS band 7 - Middle Infrared Reflectance, NDVI: Normalized Difference Vegetation Index, NDWI: Normalized Difference Water Index, LPRM: Land Parameter Retrieval Model.

Variable name	Data set/ sensor	Period used	Frequency/ wavelength/ data input	Sampling	Type	Method/ algorithm	Reference/URL
ASCAT	ASCAT	1/2007 - 12/2015	5.25 GHz	Daily, 12.5 km	Active microwave	TU-Wien change detection	Melzer (2013); Vreugdenhil et al. (2016a,b)
AMSRE_C, AMSRE_X, AMSRE_Ku	AMSR-E	1/2007 - 9/2011	6.9 GHz, 10.7 GHz, 18.7 GHz	Daily, 0.25°	Passive microwave	LPRMv06	van der Schalie et al. (2017)
AMSR2_C1, AMSR2_C2, AMSR2_X, AMSR2_Ku	AMSR2	7/2012 - 12/2015	6.9 GHz, 7.3 GHz, 10.7 GHz, 18.7 GHz	Daily, 0.25°	Passive microwave	LPRMv06	van der Schalie et al. (2017)
FLUXCOM GPP	FLUXCOM	1/2007 - 12/2015	MODIS EVI, LAI, MIR, NDVI, NDWI	8-daily, 10 km	Optical	Machine learning	Tramontana et al. (2016)
MODIS GPP	MOD17A2H v006	1/2007 - 12/2015	MODIS fAPAR	8-daily, 500 m	Optical	Semi-empirical model	Running et al. (2004); Running and Mu (2015); Zhao et al. (2005)
SIF	GOME2_F v26	1/2007 - 12/2015	740 nm	Monthly, 0.5°	Optical		Joiner et al. (2013); Joiner et al. (2014)
FLUXNET GPP	FLUXNET2015 Tier1	1/2007 - 12/2014		Daily	in situ	Eddy covariance	http://fluxnet.fluxdata.org/

onboard the meteorological operational satellite A (MetOp-A). The retrieval of daily VOD at 12.5 km sampling is based on the TU-Wien change detection model developed by Wagner et al. (1999). VOD is derived using slope and curvature of the angular backscatter dependency, which describe the volume scattering caused by vegetation (Melzer, 2013; Vreugdenhil et al., 2016a,b). The VOD retrieval uses observations from both ascending and descending mode (ascending/descending at 9:30 a.m./p.m. equatorial crossing).

2.1.2. AMSR-E VOD

AMSR-E is a passive microwave sensor measuring brightness temperature at different frequencies. VOD was retrieved using the Land Parameter Retrieval Model (LPRM) v06 (van der Schalie et al., 2017). LPRM is a radiative transfer model, which estimates VOD and soil moisture simultaneously with the use of an analytical solution based on the Microwave Polarization Difference Index (Meesters et al., 2005; Mo et al., 1982). We analyzed VOD from C- (6.9 GHz), X- (10.7 GHz) and Ku-band (18.7 GHz) obtained for descending mode (equatorial crossing at 1:30 a.m.), since the assumption in LPRM that soil and vegetation temperature are similar is best met during nighttime. Data are available at daily, 0.25° sampling.

2.1.3. AMSR2 VOD

AMSR2 measures brightness temperature both at the same frequencies as AMSR-E as well as at additional frequencies. VOD was retrieved analogously to AMSR-E using LPRM v06. In the analysis, we used VOD from

C- (C1: 6.9 GHz, C2: 7.3 GHz), X- (10.7 GHz) and Ku-band (18.7 GHz) in descending mode (1:30 a.m. equatorial crossing) at daily, 0.25° sampling.

2.2. GPP data sets

2.2.1. FLUXCOM GPP

FLUXCOM is a global GPP product that is based on upscaling site-level eddy covariance estimates of GPP by using variables from optical satellites and different machine learning algorithms including tree-based methods, regression splines, neural networks and kernel methods (Tramontana et al., 2016). For comparability with satellite VOD data, we used the satellite-based version of FLUXCOM GPP. The data set represents the median of 18 ensemble members, which consist of 9 machine learning algorithms applied to both daytime and nighttime GPP estimates. Data are available at 8-daily, 10 km sampling.

2.2.2. MODIS GPP

MODIS GPP (Running et al., 2004; Zhao et al., 2005) is based on the light-use efficiency concept introduced by Monteith (1972) in which absorbed solar energy is related to plant productivity. MODIS GPP is provided by the land product MOD17; the algorithm uses fAPAR derived from optical data for calculating the absorbed PAR (Running et al., 1999, 2000). Several versions of MOD17, differing in spatial and temporal resolution, are available. We used the MOD17A2H v006 GPP, which has 8-daily, 500 m sampling.

2.2.3. GOME-F SIF

SIF observations at 740 nm (GOME-F v26) are obtained from measurements of the Global Ozone Monitoring Experiment-2 (GOME-2) sensor flying onboard MetOp-A (Joiner et al., 2013, 2014, 2016). The retrieval algorithm of SIF proposed by Joiner et al. (2013) utilizes the filling-in of Fraunhofer lines caused by the plants chlorophyll fluorescence. Data are available at monthly, 0.5° sampling.

2.2.4. FLUXNET2015 GPP

FLUXNET2015[1] provides a compilation of in situ flux observations spread around the world. The stations measure water, heat and carbon fluxes by means of the eddy covariance method (Baldocchi, 2003). The carbon dioxide flux, i.e. net ecosystem exchange, is further partitioned into ecosystem respiration and GPP using the daytime (Lasslop et al., 2010) or nighttime (Reichstein et al., 2005) partitioning method. For our analysis, we used GPP estimates from the publicly available Tier 1 data set that were obtained with the daytime partitioning method with a variable friction velocity threshold.

2.3. Meteorological data sets

2.3.1. Precipitation

We used daily, 1° precipitation estimates from the Global Precipitation Climatology Project (GPCP) 1DD version 1.2 to aid the interpretation of the

[1]Fluxnet2015 data set (accessed June 9, 2016): `http://fluxnet.fluxdata.org//data/fluxnet2015-dataset/`

time series plot. Precipitation is estimated using a combination of satellite observations and gauge measurements (Huffman et al., 2001). The satellite data include microwave observations of frequencies above 10 GHz and infrared radiation.

2.3.2. Temperature and snow depth

Frozen conditions and snow cover lead to erroneous VOD retrievals. For this reason, we masked VOD observations using skin temperature and snow depth from ERA-Interim. ERA-Interim is a global atmospheric reanalysis produced by the European Centre for Medium-Range Weather Forecasts which incorporates a 4-dimensional variational analysis (Dee et al., 2011). Data are available at 0.7° horizontal sampling at the equator for the period from 1979 onwards.

2.3.3. Aridity Index

Since water availability is a main driver for plant growth, we analyzed results along a gradient of aridity in order to determine whether VOD-based GPP estimates perform differently in different climatic regions. The aridity index is typically calculated as the ratio of the long-term averages of potential evaporation and precipitation (Good et al., 2017; Greve et al., 2014). For computing this index, we used long-term averages of potential evaporation from the Global Land Evaporation Amsterdam Model (GLEAM; Miralles et al., 2011) v3.a (Martens et al., 2017) and precipitation from the Multi-Source Weighted-Ensemble Precipitation (MSWEP; Beck et al., 2017) v1.1

for the period 1980 to 2017. Both data sets are available at 0.25° sampling.

3. Theoretical model for estimating GPP based on VOD

For describing the relationship between VOD and GPP, we consider the following equation which relates GPP to NPP and R_a (e.g. Bonan, 2015; Odum, 1959):

$$\mathrm{GPP} = \mathrm{R_a} + \mathrm{NPP} \tag{1}$$

R_a represents the portion of the assimilates that is used by plants for their metabolism. R_a can be further separated into growth and maintenance respiration, which are proportional to the change in biomass ($\frac{dB}{dt}$) and biomass (B), respectively (Lavigne and Ryan, 1997; Ryan, 1990):

$$\mathrm{R_a} = a_0 \, \frac{d\mathrm{B}}{dt} + b_0 \, \mathrm{B} \tag{2}$$

R_a generally depends on temperature and is often modelled by assuming an exponential increase of R_a with temperature (Atkin and Tjoelker, 2003; Atkin et al., 2005; Smith and Dukes, 2013; Tjoelker et al., 2001; Vanderwel et al., 2015; Wythers et al., 2013). Consequently, the coefficients a_0 and b_0 in equation (2) are functions of temperature, although this temperature sensitivity is mainly attributed to the maintenance term of R_a (Ryan, 1990). Modelling the relationship between R_a and temperature, however, is not straight forward. Acclimation and adaptation of plants to changes in temperature further modulate the temperature sensitivity of R_a (Atkin and

Tjoelker, 2003; Gifford, 2003; Smith and Dukes, 2013; Vanderwel et al., 2015), although these two processes are acting on different time scales (Smith and Dukes, 2013). Therefore, representation of R_a in models presents a complex task (Atkin and Tjoelker, 2003; Atkin et al., 2005; Gifford, 2003; Ryan, 1991; Smith and Dukes, 2013; Vanderwel et al., 2015). For simplicity of our model, we assume that the coefficients a_0 and b_0 are independent of temperature and discuss the potential impact of this simplification in Section 6.5.

NPP is the remaining portion of the assimilates, i.e. the difference between GPP and R_a, and contains the following terms (Clark et al., 2001a,b; Girardin et al., 2010; Gower et al., 2001; Luyssaert et al., 2007):

$$\mathrm{NPP} = \frac{d\mathrm{B}}{dt} + \mathrm{VOC} + \mathrm{Herbivory} + \mathrm{Root\ exudates} \tag{3}$$

VOC stands for volatile organic compounds and are organic molecules produced by plants that are released into the ambient air. VOC may play an important role in ecology and atmospheric chemistry but constitute only a small fraction of NPP (Guenther, 2002; Kesselmeier et al., 2002). Herbivory describes the loss of above- and belowground plant biomass through animals that are feeding on these plants. Root exudates are plant-produced compounds that are released into the ground to enhance nutrient uptake or feed mycorrhiza and can also be used as a defense mechanism (Bais et al., 2006; Bertin et al., 2003; Jones et al., 2009). All these terms are not directly reflected in VOD and are thus neglected in the current model description for relating VOD to GPP. Combining equations (1)-(3) and setting $a = 1 + a_0$ and $b = b_0$, we arrive at the following differential equation for GPP:

$$\mathrm{GPP} = a \, \frac{d\mathrm{B}}{dt} + b \; \mathrm{B} \tag{4}$$

a and b represent coefficients for growth and maintenance related terms, respectively, analogous to the concept developed by Ryan (1990) for $\mathrm{R_a}$, i.e. equation (2), but now extended for GPP.

The last step in the formulation of the relationship between VOD and GPP requires a description of the relationship between VOD and biomass. This relationship, or more specifically that between VOD and aboveground biomass (AGB), is not straightforward. Liu et al. (2015) proposed an empirical, non-linear function for converting VOD to AGB using a passive merged VOD data set. Similar to this concept, but without explicitly stating the relationship between AGB and VOD, we assume that AGB can be expressed as a function of VOD:

$$\mathrm{AGB} = f(VOD) = \widetilde{VOD} \tag{5}$$

Assuming that above- and belowground terms in equation (4) are proportional, which allows to express B as a function of VOD, we arrive at the relationship between VOD and GPP, which can be described by the following differential equation:

$$\text{GPP} = a\,\frac{d\widetilde{VOD}}{dt} + b\,\widetilde{VOD} + c \tag{6}$$

c is a time-invariant offset, which is added from a mathematical point of view and does not necessarily reflect the neglected terms in equation (3) but rather aids the conversion of VOD to GPP if the offset is not already included in $f(VOD)$.

Equation (6) presents the theoretical concept in this study, which we aim to model for different VOD data sets through the use of GAM (Hastie and Tibshirani, 1987).

4. Methods

4.1. Generalized Additive Models

GAM is a regression approach which can utilize different link functions for fitting a limited set of predictor variables ($\mathbf{x}$) against the expected value of the response variable (y) (Hastie and Tibshirani, 1987). For calculating the conditional expected value ($\mathbb{E}[y \mid \mathbf{x}]$), the algorithm requires specification of the data distribution for the response variable. The approach allows non-linear and non-monotonic relationships between a response variable and predictor variables, which are represented by fitting smooth spline functions (f) for each predictor (Hastie and Tibshirani, 1987, 1990). As such, GAM does not require specification of the underlying relationship between predictor and response variable. Since we do not explicitly know the shape of the relationship between biomass and each VOD data set, GAM presents a suitable method in this study for estimating GPP based on VOD.

For the analysis, we used LinearGAM from the python package pygam (Servén et al., 2018), which uses the normal distribution together with the identity as link function. In this case, GAM with p input variables has the form (Hastie and Tibshirani, 1987):

$$\mathbb{E}\big[y \mid \mathbf{x}\big] = \alpha + \sum_{j=1}^{p} f_j(x_j) \tag{7}$$

We used LinearGAM with 25 splines of order 3, which allows variability in the shape of the fitted spline across the data range, together with a value of 200 for the smoothing parameter lambda, which provides strong smoothing to ensure generalizability.

We applied GAM by fitting different sets of input variables against global or in situ GPP estimates. To indicate which set of input variables was used for training GAM, we refer to the model as GPP() with a list of input variables in parenthesis. For example, GPP(VOD, ΔVOD) denotes a GAM setup that uses VOD and ΔVOD as input.

4.2. Experimental setups

Our analysis comprises three experiments. The first experiment assesses the model's performance in temporal extrapolation, while the second experiment evaluates the model's capability in spatial extrapolation using cross validation and model selection. These experiments allow to determine the model's performance during periods or at locations it has not been trained on, which relates to the situation during the upscaling of in situ GPP assessed in the third experiment.

4.2.1. Testing temporal extrapolation

For testing the model's ability to reproduce the temporal dynamics of GPP, we trained GPP(VOD, ΔVOD) at each grid cell against the global GPP from FLUXCOM. The comparison with an existing global GPP product has the advantage of minimizing the impact of scale differences, which are often observed for in situ observations versus satellite data. It can thus demonstrate if the model can be used in general for estimating GPP. For the analysis, we split the data in time using the first two years of each data set for training the model (AMSR-E, ASCAT, SIF: 1/2007 to 12/2008; AMSR2: 7/2012 to 6/2014) and the remaining period for testing (AMSR-E: 1/2009 to 9/2011; ASCAT, SIF: 1/2009 to 12/2015, AMSR2: 7/2014 to 12/2015). To support global results, we repeated the analysis using in situ FLUXNET observations. For this setup, AMSR2 data are omitted since the overlap period with FLUXNET extends only through 2014.

In addition to the analysis of GPP(VOD, ΔVOD), we determined the added value of using the combination of VOD and ΔVOD compared to VOD or ΔVOD alone. The reason for treating VOD and ΔVOD separately against our proposed theory, was to exclude the possibility that either signal alone is able to match the GPP signal merely by applying a non-linear regression like GAM.

4.2.2. Testing spatial extrapolation using cross validation and model selection

Using leave-site-out cross validation with FLUXNET GPP as target variable, we assessed the model's ability for spatial extrapolation. For each site, GPP(VOD, ΔVOD) or GPP(SIF) was trained with data from all sites except the site under evaluation. The model was then applied to the data that was left out and compared against the target variable. As the data were split in space, the training and testing period each span the full overlap period with FLUXNET for each data set. Apart from the full signal, we also assessed the performance of anomalies of the resulting GPP estimates in order to evaluate the strength of the relationship in the absence of seasonality. Anomalies were calculated as differences to the mean seasonal cycle during the testing period for the VOD- or SIF-based GPP estimates (i.e., after model application) and FLUXNET GPP.

We further assessed if the additional use of the temporal grid cell median of each data set ($mdnVOD$ or $mdnSIF$) can improve the spatial extrapolation of the model, i.e. GPP(VOD, ΔVOD, $mdnVOD$) or GPP(SIF, $mdnSIF$). $mdnVOD$ is a static component for each data set, which varies with each grid cell and thus does not contribute to the temporal dynamic of the resulting estimate. $mdnVOD$ identifies areas of similar biomass and thus further relates to land cover, since grassland generally has a lower biomass than shrubland, which in turn has a lower biomass than a dense forest. In contrast, $mdnSIF$ identifies areas of similar photosynthetic activity and therefore reflects a different property than $mdnVOD$.

To assess whether an improvement in model performance can be attributed to a gain in information through the addition of the respective variable or is caused by an additional degree of freedom, we computed the Akaike Information Criterion (AIC; Akaike, 1974). For this analysis, we randomly split the station data into two data sets. We used one half of the stations for training and the remaining half for testing.

4.2.3. Upscaling

In the third experiment, we estimated GPP globally based on VOD using the best performing model setup as assessed during cross validation and model selection. The upscaling was performed similarly to cross validation with the difference that the model for each setup was trained against all available in situ FLUXNET GPP. After applying the model to the global VOD data sets, we evaluated the model's performance by comparing the VOD-based GPP estimates with global GPP estimates from FLUXCOM and MODIS. For the analysis of mean annual GPP, we additionally performed an uncertainty analysis to determine the influence of the choice of the stations on the GPP estimation. For this, we repeated the VOD-based upscaling ten times, each time reducing the number of stations by 10%. The excluded stations were randomly drawn without replacement. Therefore, each model run in the uncertainty analysis is based on data from 90% of the stations.

4.3. Data preparation

The analysis is based on two different resolutions: for the comparison between VOD, FLUXCOM and MODIS data, the common sampling is 8-daily, 0.25° while for the comparison with SIF, the common sampling is monthly, 0.5°. We aggregated data sets with a higher resolution using the average over 8 days or the average over the grid cell. For data sets with a lower spatial resolution like snow depth and temperature data, we performed nearest neighbor resampling.

VOD observations were masked when temperature was below 0°C and snow cover was present. The masking was also applied to GPP data sets for comparability. In addition to snow and temperature masking, VOD from passive sensors was masked for radio frequency interference using the accompanying flags, since it can also lead to erroneous retrievals of VOD (Li et al., 2004; Njoku et al., 2005).

We approximate the derivative of VOD at each grid cell ($\mathbf{x}_i$) with the change of the smoothed VOD signal between two consecutive VOD observations:

$$\Delta VOD(\mathbf{x}_i, t_j) = VOD(\mathbf{x}_i, t_j) - VOD(\mathbf{x}_i, t_{j-1}) \tag{8}$$

The smoothing was computed using a Savitzky-Golay filter (Savitzky and Golay, 1964) with a window size of 11 time steps for 8-daily data and 5 time steps for monthly data. The window size for each resolution was chosen after visual inspection of the smoothed time series at the location of the FLUXNET sites. Additionally, we performed a cross validation similar to the temporal extrapolation experiment for 8-daily AMSRE_X and for GPP(VOD, ΔVOD) but using different window sizes during the computation of ΔVOD (Figs. S3). Results for Spearman correlation and $RMSE$ confirmed that a window size of 11 time steps is a suitable choice presenting a trade-off between a preferably high median correlation, low median $RMSE$ and still relatively low window length.

During cross validation, we additionally assessed the performance of the GPP anomalies relative to the mean seasonal cycle. We calculated anomalies for sites with more than two years of data using the python package pytesmo (Paulik et al., 2015).

4.4. Statistical analysis

Prior to the analysis, we tested if grid cell data of the global data sets follow normal distribution using the D'Agostino and Pearson's test (D'Agostino, 1971; D'Agostino and Pearson, 1973). We found that on average 75% of the grid cells differ from normal distribution. For this reason, we calculated the non-parametric Spearman rank correlation and used the temporal grid cell median instead of the mean in the analysis.

We evaluated model performance by calculating the Spearman rank correlation coefficient (r) and root mean square error ($RMSE$). For the leave-site-out cross validation, we additionally analyzed the index of agreement

(IoA), which is a standardized measure for the model prediction error and is defined after Willmott (1981) as:

$$IoA = 1 - \frac{\sum_{i=1}^{n}(p_i - o_i)^2}{\sum_{i=1}^{n}(\mid p_i - \bar{\mathbf{o}} \mid + \mid o_i - \bar{\mathbf{o}} \mid)^2} \quad \text{with } n = \text{number of observations} \quad (9)$$

where p represents the model output and o the in situ observations. The index ranges between 0 (worst agreement) and 1 (best agreement).

For model selection, we computed AIC using the python package RegscorePy[2]. AIC is a relative measure for the goodness of fit for different model setups while penalizing higher numbers of input variables (Akaike, 1974). The model setup with the lowest AIC is then considered as the optimal choice.

5. Results

5.1. Temporal extrapolation

The application of GAM for each grid cell is illustrated for a grid cell dominated by rainfed cropland in Fig. 1. In this example, GPP(VOD, ΔVOD) is able to capture the temporal dynamics of FLUXCOM GPP (Fig. 1a). In contrast, VOD shows a positive temporal lag with respect to GPP (Fig. 1b), while ΔVOD results in a negative lag with GPP. Making use of both VOD and ΔVOD, the model can largely compensate the observed lags for the individual signals of VOD and ΔVOD.

[2]RegscorePy v1.0: `https://pypi.org/project/RegscorePy/`

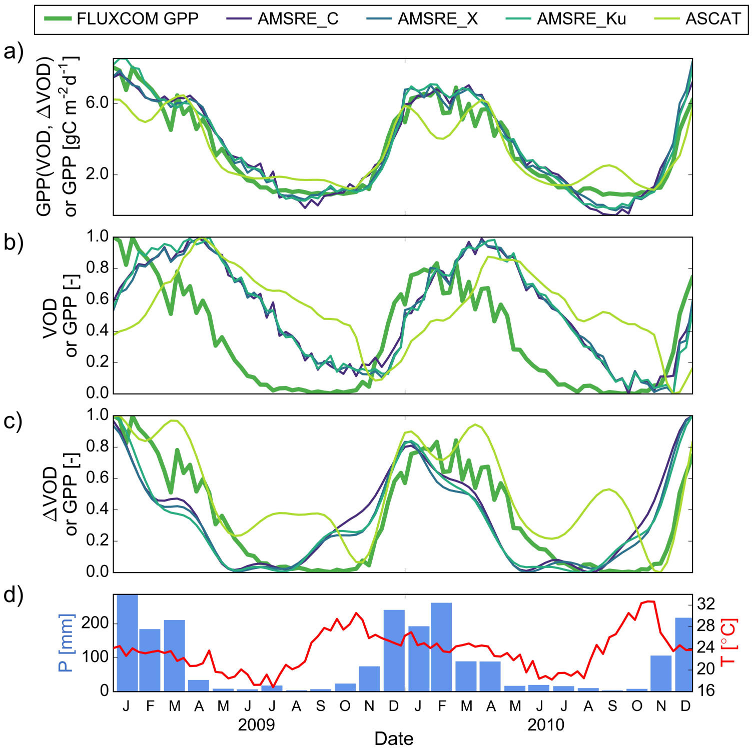

Figure 1: Time series plot for a grid cell dominated by rainfed cropland (35.125°E, 15.125°S) for different VOD data sets for the period 1/2009 to 12/2010: 8-daily FLUXCOM GPP and a) GPP(VOD, ΔVOD), b) VOD and c) ΔVOD. GPP(VOD, ΔVOD) was trained at this grid cell against FLUXCOM data for the period 1/2007 to 12/2008. Data in (b) and (c) are scaled between 0 and 1 to aid visual comparison of the temporal dynamics. (d) Monthly precipitation and 8-daily surface temperature.

Applying the model per grid cell globally at 8-daily, 0.25° sampling, the resulting GPP estimates show high temporal agreement with FLUXCOM GPP (Fig. 2). Correlations are higher for passive VOD data sets (0.69 $\leq$ median $r \leq$ 0.72) than for the active VOD data set (median r=0.61). For passive VOD data sets, correlations are especially high over Africa, parts of Australia and Europe. For the active VOD, high correlations are observed over Europe, North America and parts of South America. Consistent with the correlation results, $RMSE$ (Fig. S4) yields lower global median values for passive VOD data sets (0.85 $\leq$ median $RMSE \leq$ 0.88 $gCm^{-2}d^{-1}$) than for the active VOD (median $RMSE$=0.99 $gCm^{-2}d^{-1}$). Comparing the different frequencies of the passive VOD data sets, Ku-band results in the lowest median $RMSE$ closely followed by X-band. Regions with lowest $RMSE$ are observed over Australia for all VOD data sets, while regions with highest $RMSE$ are found mainly in northern latitudes.

The correlations increase for all data sets when performing the analysis at monthly, 0.5° sampling (Table S2), yielding median r between 0.80 and 0.82 for passive VOD and 0.74 for the active VOD. When repeating the analysis using either VOD or ΔVOD alone as input, we found that GPP(VOD, ΔVOD) outperforms GPP(VOD) and GPP(ΔVOD) at both resolutions (Table S2) with an average difference in median r of about 0.1 and 0.2 for GPP(VOD) and GPP(ΔVOD), respectively. The different frequencies of AMSR-E generally yield similar results. However, X-band data consistently showed the highest correlation at both resolutions. This finding was also observed for AMSR2 frequencies (Table S2). Compared with correlations obtained for SIF (median r=0.73), GPP(VOD, ΔVOD) at monthly, 0.5° sampling shows comparable or slightly higher median correlations for active and passive VOD, respectively.

The added value of combing VOD and ΔVOD can be further confirmed using in situ FLUXNET GPP. Correlations for GPP(VOD, ΔVOD) are higher than for the individual signals, i.e. GPP(VOD) and GPP(ΔVOD) (Fig. S5) with an average increase in median r of about 0.1 and 0.3 for GPP(VOD) and GPP(ΔVOD), respectively. Comparing median correlations of the in situ analysis with those obtained in the global comparison, the median r for SIF yields almost the same value (0.73 obtained for global GPP compared to 0.72 for in situ GPP). For VOD data sets, however, median r for the in situ analysis is on average lower by 0.1 than for the global comparison.

These results, especially for the global comparison, demonstrate the model's capability in temporal extrapolation and support our theory of representing the relationship between VOD and GPP with a differential equation.

5.2. Spatial extrapolation

Using leave-site-out cross validation, we evaluated the performance in spatial extrapolation of the relationship between VOD and GPP. For the full signals (Fig. 3, S6 and S7), the performance for SIF is generally higher than for VOD data. Median values of IoA and r are comparable to or lower for

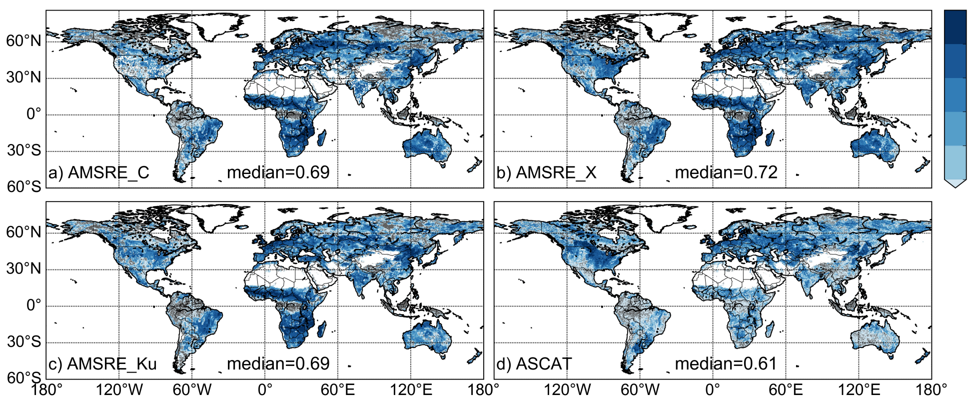

Figure 2: Spearman rank correlation (r) between FLUXCOM GPP and GPP(VOD, ΔVOD) for different VOD data sets for the testing period (AMSR-E: 1/2009 to 9/2011; ASCAT: 1/2009 to 12/2015). The analysis is based on data at 8-daily and 0.25° sampling. GPP(VOD, ΔVOD) is trained at each grid cell separately against FLUXCOM using data from the period 1/2007 to 12/2008. Correlations that are not significant ($p>0.05$) are masked in grey. The median values denote the median of significant correlations for each data set.

VOD than for SIF, while median $RMSE$ is higher for VOD than for SIF in all cases. The addition of the temporal median as input to GAM does not appear to have the same effect for VOD and SIF. While the performance for VOD increases when adding $mdnVOD$, SIF does not appear to benefit from including $mdnSIF$ since the correlations do not differ markedly between GPP(SIF) and GPP(SIF, $mdnSIF$). For VOD, however, the increase in performance upon adding $mdnVOD$ indicates that the offset, which is already implicitly included in GAM, is not a globally constant value but instead varies for each grid cell. The relationship between VOD and GPP thus is additionally modified by a static component of vegetation biomass within a grid cell as represented by $mdnVOD$. In contrast, the offset in the relationship between SIF and GPP presents a global value and does not vary with $mdnSIF$.

Results for the anomalies of the VOD- or SIF-based GPP estimates (Fig. 4, S8 and S9) reveal a slightly higher performance for VOD than for SIF. Median values of IoA and r are comparable or in some cases higher for VOD than for SIF, while median $RMSE$ is lower for VOD than for SIF in all cases. Including the temporal median does not affect the metrics except for IoA for VOD. In this case, the anomalies for GPP(VOD, ΔVOD, $mdnVOD$) result in slightly higher IoA values than for GPP(VOD, ΔVOD).

For the different AMSR-E frequencies, the cross validation results further reveal that X-band data result in higher performance than C- and Ku-band data in most cases, which is especially true for data at 8-daily, 0.25° sampling.

The two extrapolation experiments for the full signals further show that correlations for the spatial extrapolation (Fig. 3) are generally lower than for the temporal extrapolation (Fig. S5). Even when adding $mdnVOD$, median r during spatial extrapolation is on average lower by about 0.1 than during temporal extrapolation at both resolutions. Similarly, SIF also experiences a reduction in correlation during spatial extrapolation compared to temporal extrapolation. The difference in median r, however, is about 0.05 and thus smaller than for VOD. This indicates that the reduction in performance for VOD data is not alone caused by the model representation itself but is also strongly affected by scale differences between point measurements and the spatial coverage of the grid cell data.

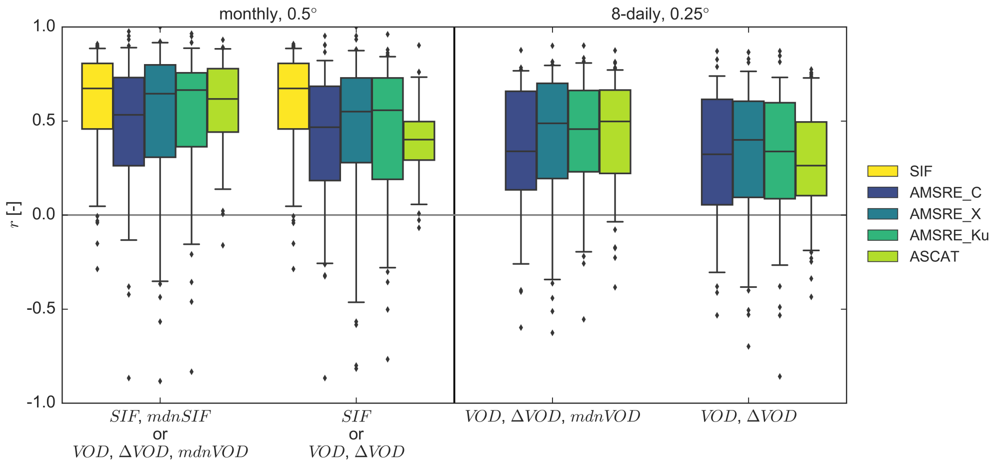

Figure 3: Leave-site-out cross validation for Spearman rank correlation (r) at monthly, 0.5° and 8-daily, 0.25° sampling. The analysis is based on the full signals of in situ FLUXNET GPP and GPP estimates based on VOD or SIF. Labels on the x-axis indicate which input variables are used for each model. Box plot whiskers extend to the 5th and 95th data percentile. Abbreviations – $mdnSIF$: temporal grid cell median SIF; ΔVOD: temporal change in VOD between two consecutive observations; and $mdnVOD$: temporal grid cell median VOD.

Cross validation results for the full signals for AMSR2 (Fig. S10, S11 and S12) are generally similar to those obtained for AMSR-E. AMSR2 frequencies, however, show a slight decrease in performance for r and IoA and a slight increase in performance for $RMSE$ compared to AMSR-E frequencies (Fig. S12). Consistent with AMSR-E data, AMSR2 X-band often shows higher performance than the remaining frequencies.

The previous results suggest that the combination of all three input variables, i.e. VOD, ΔVOD and $mdnVOD$, can improve model performance. Results of AIC for the different model setups relative to AIC for GPP(VOD, ΔVOD, $mdnVOD$) in Fig. 5 further confirm this finding. For all VOD data sets at both resolutions, the combination of VOD and ΔVOD yields lower

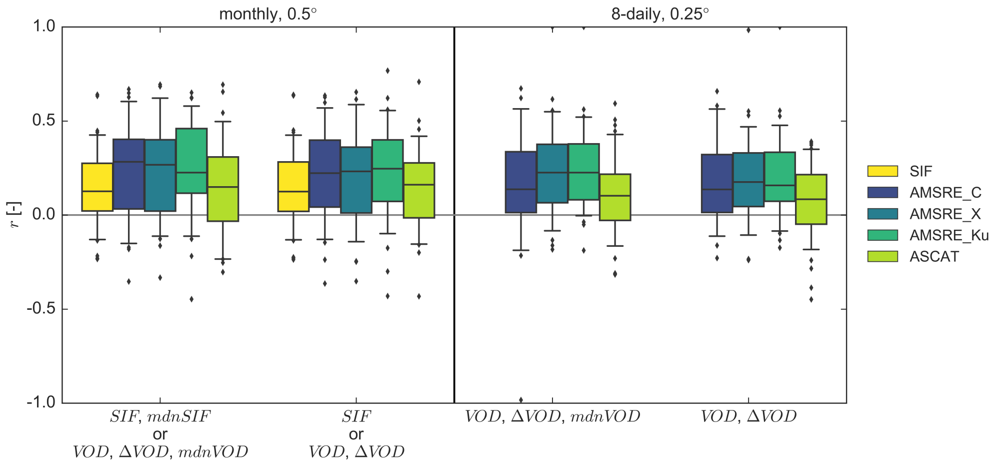

Figure 4: As Fig. 3 but for the anomalies of in situ FLUXNET GPP and GPP estimates based on VOD or SIF.

AIC values than for each input variable alone. When adding $mdnVOD$, AIC is further reduced in the majority of cases. Exceptions from this rule are found for AMSRE_C and AMSRE_X at 8-daily, 0.25° sampling, where the use of all three variables increases AIC. Since this finding is not consistent with results at monthly, 0.5° sampling for the same frequencies, we suspect that this might be an artifact of the choice of stations. We thus still suggest the use of all three variables for upscaling GPP based on VOD data. In case of SIF, the difference in AIC between GPP(SIF) and GPP(SIF, $mdnSIF$) is negligible. This confirms that, unlike for VOD, the relationship between SIF and GPP does not depend on the data set median.

5.3. Upscaling of in situ GPP

Based on the results for cross validation and model selection, we used GPP(VOD, ΔVOD, $mdnVOD$) for the global upscaling with VOD and

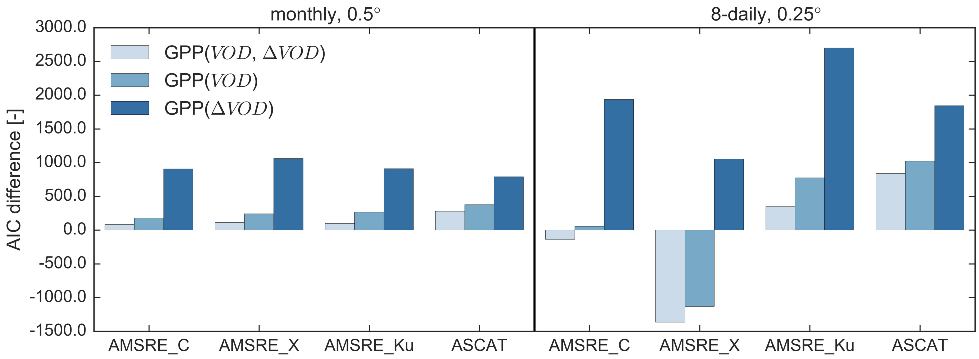

Figure 5: Difference in AIC between model setups with respect to AIC for GPP(VOD, ΔVOD, $mdnVOD$) for each VOD data set. For SIF, the AIC difference between GPP(SIF) and GPP(SIF, $mdnSIF$) is very low (1.67) compared with VOD data sets and therefore not displayed. The analysis is based on data at monthly, 0.5° or 8-daily, 0.25° sampling. Positive values indicate model improvement when using all three variables as input compared to models with a lower number of input variables.

GPP(SIF) for the upscaling with SIF for further analysis. We will put an emphasis on the output from X-band due to the overall better performance during the temporal and spatial extrapolation experiments.

5.3.1. Relationship between VOD and GPP

The partial dependence plots for GPP(VOD, ΔVOD, $mdnVOD$), which are examplified for AMSRE_X in Fig. 6, demonstrate the contribution of the three input variables to the model. For all VOD data sets, we observed that the functions for VOD and ΔVOD mainly increase, while the function for $mdnVOD$ decreases. The increase for ΔVOD is true for the region where the majority of data are located and the confidence interval is small. For AMSRE_X, this region ranges between -0.3 and 0.4 (Fig. 6e). The inverse relationship between VOD and $mdnVOD$ and the additive linking of variables

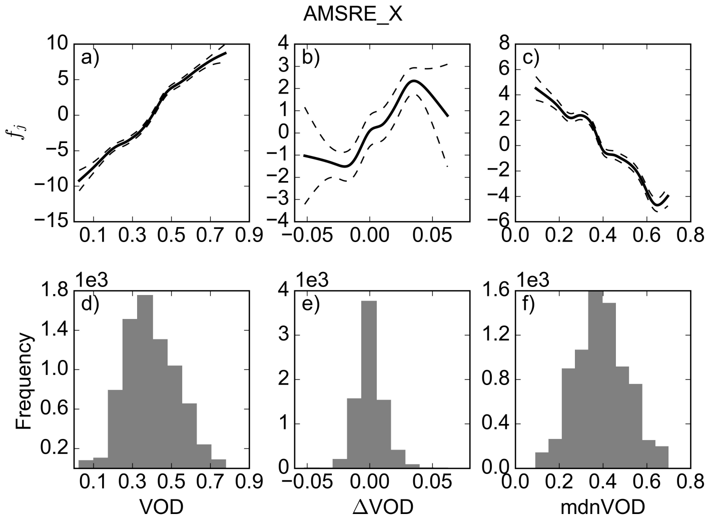

Figure 6: GAM Partial dependence plots for GPP(VOD, ΔVOD, $mdnVOD$) obtained during upscaling (a-c) and histogram of input variables (d-f) for AMSRE_X at 8-daily and 0.25° sampling. Dashed lines in (a-c) indicate the confidence intervals.

in GAM suggest that $mdnVOD$ is subtracted from VOD.

5.3.2. Global correlation of upscaled GPP

Results for GPP(VOD, ΔVOD, $mdnVOD$) at 8-daily, 0.25° sampling show moderate temporal agreement with FLUXCOM and MODIS GPP (Fig. 7). Median r ranges between 0.54 and 0.62 for FLUXCOM and between 0.52 and 0.60 for MODIS. The correlations also include some negative values (Fig. S13). For significant correlations, the fraction of negative correlations lies between 5 to 9% for passive VOD and about 12% for active VOD. Highest median correlations are observed for X-band data, which is consistent with the results from temporal and spatial extrapolation. At monthly, 0.5° sampling, the global median r increases, ranging between 0.67 and 0.71 for

FLUXCOM and between 0.66 and 0.70 for MODIS. For GPP(SIF), median r reaches 0.71 for FLUXCOM and 0.66 for MODIS.

Results for AMSR2 frequencies (Fig. S15) are generally similar to those obtained for AMSR-E, although AMSR2 frequencies yield slightly lower median correlations than AMSR-E frequencies.

Comparing correlations with FLUXCOM between the upscaling and the global temporal extrapolation (Section 5.1), median r for SIF is similar. For VOD, however, correlations for the upscaling are markedly lower than during temporal extrapolation, which is consistent with the reduction in model performance during cross validation.

5.3.3. Comparison of annual GPP

In addition to assessing the temporal dynamics, we compared mean annual GPP for GPP(VOD, ΔVOD, $mdnVOD$) from AMSRE_X with mean annual GPP for FLUXCOM and MODIS. The analysis is based on data points where all three data sets are available. In general, GPP(VOD, ΔVOD, $mdnVOD$) shows the expected spatial pattern with highest values observed in tropical regions (Fig. 8a). Nevertheless, GPP(VOD, ΔVOD, $mdnVOD$) for AMSRE_X tends to overestimate annual GPP in many regions compared to FLUXCOM and MODIS (Fig. 8b-c). Closest agreement between AMSRE_X and FLUXCOM or MODIS is observed for tropical regions. Consistent with these results, we observed lowest differences between AMSRE_X and FLUXCOM or MODIS at low aridity (Fig. 9), which represents very

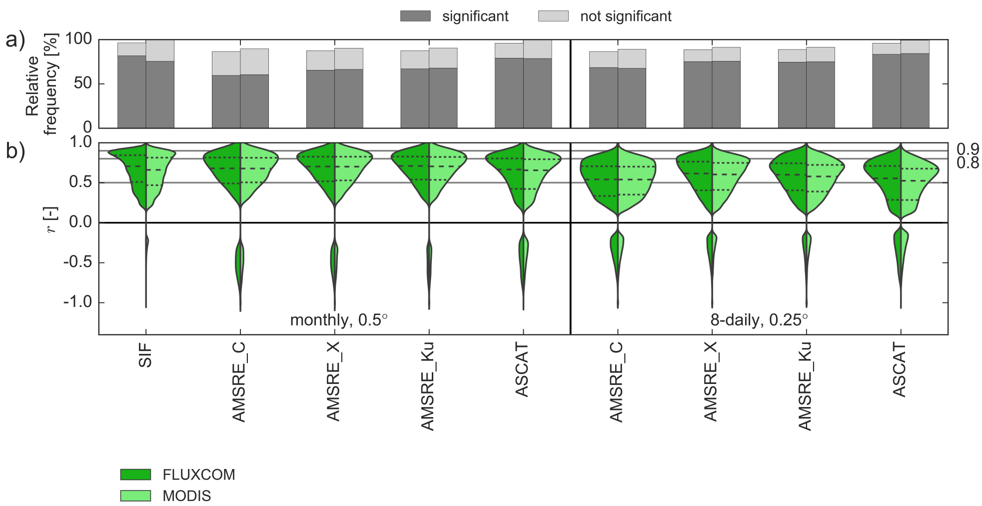

Figure 7: Spearman rank correlation (r) between GPP data sets (FLUXCOM, MODIS) and upscaling for GPP(VOD, ΔVOD, $mdnVOD$) or GPP(SIF). Data were trained against in situ GPP estimates (FLUXNET) at 8-daily, 0.25° or monthly, 0.5° sampling. a) Relative frequency of grid cells with significant and not significant correlations with respect to all possible land grid cells at each resolution. Areas that do not contain results relate to gaps obtained during masking for radio frequency interference or to not produced pixels in the original data products. b) Violin plot of significant correlations. Horizontal grey lines indicate correlation values of 0.5, 0.8 and 0.9. Dashed lines indicate the median (long dashes) and the 25th and 75th percentile (short dashes).

humid regions like the tropics. Under mesic conditions, differences between products are slightly higher than for very dry or very humid regions.

The observed overestimation is also apparent in the zonal mean (Fig. 8d). GPP(VOD, ΔVOD, $mdnVOD$) consistently overestimates annual GPP from FLUXCOM and MODIS and is closest to FLUXCOM and MODIS near the equator. Despite the overestimation, GPP(VOD, ΔVOD, $mdnVOD$) shows similar latitudinal features as for FLUXCOM and MODIS. The uncertainty analysis of GPP(VOD, ΔVOD, $mdnVOD$) for AMSRE_X further demonstrates that the choice of stations for the upscaling has an effect on the GPP estimation (Fig. 8d). The range of the ten model runs is larger in the tropics and the southern hemisphere than in the northern hemisphere, which is caused by differences in station density in these regions. The map of the standard deviation for the ten model runs (Fig. S16) shows that differences between the model runs are most pronounced in the tropics, the Sahel, southern parts of Africa and large parts of Australia.

GPP(VOD, ΔVOD, $mdnVOD$) for AMSR2_X results in a higher agreement with FLUXCOM and MODIS than for AMSRE_X. In contrast to AMSRE_X, AMSR2 yields smaller differences in annual GPP with FLUXCOM and MODIS (Fig. S17a-c), which is in line with the smaller $RMSE$ observed for AMSR2 during cross validation. Annual GPP for AMSR2, however, also exhibits areas where FLUXCOM and MODIS are underestimated, which are located mainly in the Sahel and Australia. The latitudinal distribution of annual GPP (Fig. S17d) shows that AMSR2_X overall yields a closer agreement between with FLUXCOM or MODIS than for AMSRE_X. Similar as for AMSRE_X, AMSR2_X deviates less from FLUXCOM and MODIS in the tropics.

6. Discussion

6.1. Relationship between VOD and GPP

Our study presents a model for estimating GPP based on VOD, which describes the relationship between VOD and GPP through a differential equation. The model uses different VOD variables, i.e. VOD, ΔVOD, and $mdnVOD$, as input. The approach is based on the assumption that VOD provides an estimate for aboveground living biomass (Liu et al., 2011, 2015), which has been employed by multiple studies for detecting trends in biomass (Andela et al., 2013; Liu et al., 2013b,a, 2015; Marle et al., 2016). In support of this theory, Tian et al. (2016) have demonstrated the applicability of the biomass-VOD relationship in a dryland ecosystem.

The relationship between biomass and VOD, however, is rather complex. Since VOD presents a measure of vegetation water content (Jackson and Schmugge, 1991), it can also be considered as the product of biomass and relative water content (Momen et al., 2017), a quantity that is closely related to the water potential of vegetation (Barnard et al., 2011; Brodribb and Holbrook, 2003; Momen et al., 2017). For this reason, VOD has also been used as a surrogate for fuel moisture in fire modelling (Forkel et al., 2017) or for leaf water potential and isohydricity of vegetation (Konings and Gentine, 2016;

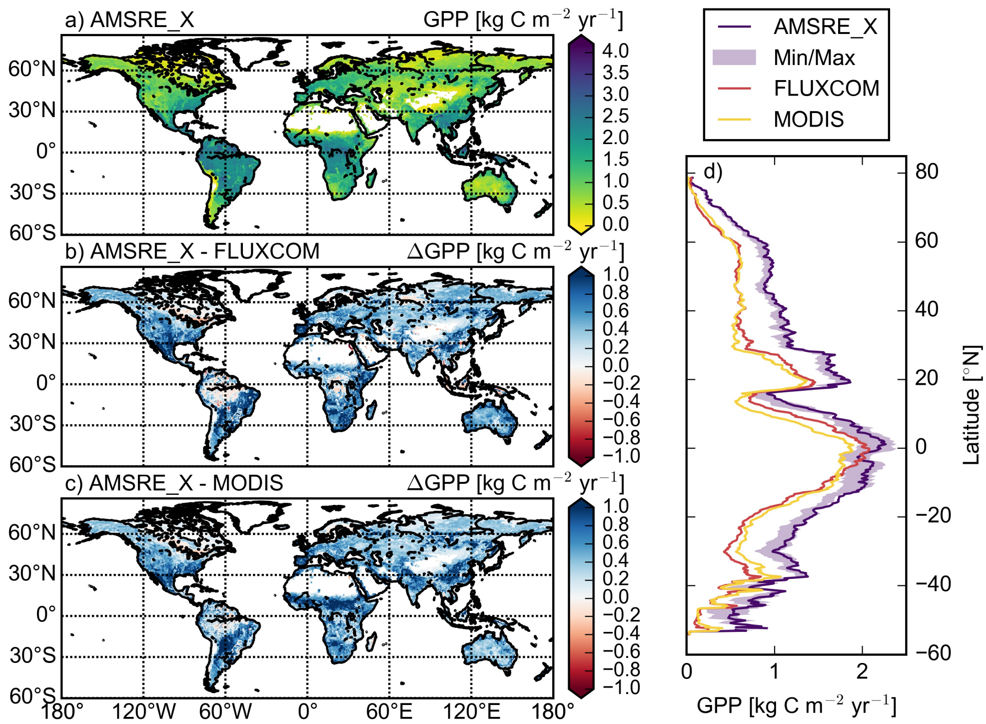

Figure 8: Mean annual GPP for the period 2007 to 2010: a) upscaling of GPP(VOD, ΔVOD, $mdnVOD$) for VOD AMSRE_X, b) difference in mean annual GPP between FLUXCOM and AMSRE_X c) difference in mean annual GPP between MODIS and AMSRE_X. Values in (b) and (c) are displayed between -1 and 1. d) Zonal mean of mean annual GPP. Estimates for GPP(VOD, ΔVOD, $mdnVOD$) were produced using data at 8-daily, 0.25° sampling. The area denoted by Min/Max represents the minimum and maximum of the zonal means for the ten model runs obtained during the uncertainty analysis for GPP(VOD, ΔVOD, $mdnVOD$) with VOD AMSRE_X.

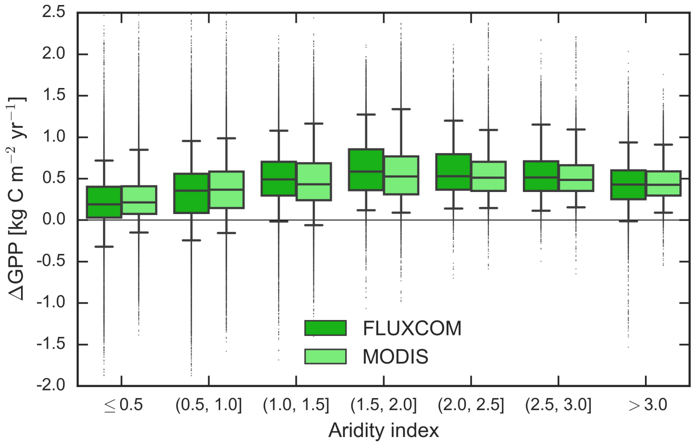

Figure 9: Differences in mean annual GPP between AMSRE_X and FLUXCOM or MODIS stratified along the aridity index. The analysis is based on the period 2007 to 2010 and uses 8-daily, 0.25° data. Mean annual GPP for AMSRE_X is computed using GPP(VOD, ΔVOD, $mdnVOD$). Box plot whiskers represent the 5th and 95th data percentile.

Konings et al., 2017a,b). The impact of the relative water content on the relationship between biomass and VOD, however, is not entirely clear. Using in situ estimates of leaf water potential, Momen et al. (2017) have shown that variations in VOD are largely driven by changes in leaf water potential or the interaction of leaf water potential and LAI rather than LAI alone. Nevertheless, studies connected leaf water potential to maximum stomatal conductivity (Klein, 2014; Running, 1976). Since stomatal conductivity controls photosynthesis by regulating the CO_2 uptake (e.g. Damour et al., 2010), this can provide an additional indication for the potential use of VOD to estimate GPP. Considering VOD as a proxy for leaf water potential, however, cannot explain the increase in temporal agreement when combining the original VOD signal and its derivative as observed in our study. Therefore, we propose that in our context VOD presents an estimate of the metabolically active biomass.

6.2. Impact of VOD frequency on the relationship with GPP

We observed that VOD data from X-band appear to be a suitable predictor for estimating GPP. This finding may be counter-intuitive since VOD from lower frequencies (i.e. longer wavelengths), such as L-band, rather than from higher frequencies was demonstrated to correlate closely with total aboveground vegetation biomass (Rodríguez-Fernández et al., 2018). Total aboveground biomass, however, is a rather poor predictor of GPP due to the presence of large-size plant parts functioning as structural components that are less metabolically active (Litton et al., 2007). This is in accordance with observations of lower correlations between VOD and GPP for L-band than for C- or X-band VOD (Teubner et al., 2018). In contrast, the metabolically active plant parts, i.e. leaves and fine roots, present a suitable estimator for GPP (Litton et al., 2007). Since metabolically active cells contain water, the use of VOD in our model can present a suitable proxy for the aboveground metabolically active parts, which in turn can be related to GPP. In addition to this, Litton et al. (2007) demonstrated that in forests the partitioning of carbon to leaves is a constant fraction of GPP. This implies that total GPP can be obtained by estimating the portion of GPP that goes into the leaf compartment. Those two concepts together with the theoretically stronger sensitivity of higher VOD frequencies to small vegetation parts, i.e. leaves and small structural components (Woodhouse, 2005), can explain why high frequency VOD rather than low frequency VOD is suited for retrieving GPP.

6.3. Extrapolation of VOD-GPP relationship

In both extrapolation experiments (temporal and spatial), we observed a lower agreement of VOD-based estimates with in situ GPP than with global GPP. In contrast, SIF only showed a slight reduction in performance during spatial extrapolation. This indicates that subpixel heterogeneity plays a more important role for the relationship between VOD and GPP than between SIF and GPP. From a mathematical point of view, the relationship between VOD and GPP strongly depends on the appropriate weighting of the two dynamic terms in the model, VOD and ΔVOD, in order to match the temporal dynamic of the reference GPP. Since variations in the weighting result in a temporal shifting of the VOD-based GPP estimate, weights that are not representative for the respective grid cell may decrease model performance. Therefore, scale differences potentially have a stronger impact on the upscaling of GPP with VOD than with SIF.

For the spatial extrapolation experiment, we further found that the offset in the VOD-GPP relationship varies between grid cells, unlike for the SIF-GPP relationship for which the offset is a global value. The reason for this may be linked to the contribution of structural components to VOD. VOD contains information both on woody and leaf parts (Tian et al., 2017). For estimating total GPP, however, the relevant aboveground information are mainly the leaves (Litton et al., 2007). Larger plant parts, which also contribute to the VOD signal, exhibit lower metabolic activity than leaves (Litton et al., 2007). Adding $mdnVOD$ as input to GAM thus seems to ensure that structural components within the grid cells are subtracted, thereby making the remainder more closely related to the leaves. When considering longer periods, the static $mdnVOD$ should thus be replaced with a metric that varies over time in order to reflect changes in land cover.

The extrapolation experiments overall indicated that further input variables may be needed to enhance the model's extrapolation capability. Including land cover information, which is commonly used in upscaling of in situ GPP (Chen et al., 2010; Jung et al., 2009; Tramontana et al., 2015, 2016), may help reduce the impact of scale differences. A second variable, which may improve extrapolation, is the fraction of C3, C4 and CAM plants within a grid cell. These plants employ different strategies for carbon uptake and, hence, have a different efficiency in photosynthesis (e.g. Bonan, 2015). In turn, this may alter the VOD-GPP relationship.

6.4. Performance of GPP upscaling

The VOD-based upscaling of GPP generally compared well with GPP from FLUXCOM and MODIS. Some areas exhibit inverse temporal dynamics with GPP. This, however, is not an issue of the model formulation but of the VOD observations itself. Microwave VOD observations can exhibit an inverse relationship to optical vegetation parameters in wet regions for passive

VOD and in dry regions for active VOD (Jones et al., 2011; Liu et al., 2011; Vreugdenhil et al., 2016b). Without explicitly accounting for this behavior, these patterns of negative correlations are propagated through to the VOD-based GPP estimates.

Considering annual GPP, we observed a closer agreement with GPP from FLUXCOM and MODIS for X-band VOD from AMSR2 than from AMSR-E. On the one hand, this finding may be linked to differences between the sensors themselves. Du et al. (2017) reported that small differences between the performance for AMSR-E and AMSR2 exist. In line with this, we observed lower RMSE for AMSR2 than for AMSR-E during cross validation. On the other hand, the differences between AMSR-E and AMSR2 could also be caused by the different analysis periods. Considering that the temporal coverage of FLUXNET stations varies for AMSR-E and for AMSR2, this likely has the same effect as seen for the uncertainty analysis, because stations used for upscaling AMSR-E were not necessarily present in the period for AMSR2, and vice versa. The reason for these differences still requires further investigation.

Apart from methodological differences between the VOD-based GPP estimation and GPP from FLUXCOM or MODIS, further variations may arise from differences in the setup. FLUXCOM and MODIS GPP products both have a higher spatial resolution than VOD data, which potentially reduces the impact of scale differences. The FLUXNET data set used for the upscaling in FLUXCOM also differs in the data period and incorporates a larger number of sites (Tramontana et al., 2016). As shown for the uncertainty analysis, the choice of FLUXNET stations has an impact on the VOD-based upscaling and, thus, likely contributes to observed differences between VOD-based GPP and FLUXCOM GPP. In addition, FLUXCOM and MODIS incorporate ancillary information on land cover (Running et al., 1999; Tramontana et al., 2016), which was already discussed in Section 6.3 as possibility for model improvement.

6.5. Impact of model simplifications

The framework neglects the temperature dependency of R_a, which is often represented as an exponential increase of R_a with temperature (Wythers et al., 2013; Vanderwel et al., 2015; Tjoelker et al., 2001; Smith and Dukes, 2013; Atkin et al., 2005; Atkin and Tjoelker, 2003). Not accounting for this effect thus may explain the observed overestimation of the VOD-based GPP estimates. The comparison of estimates from AMSR-E and AMSR2, however, showed a closer agreement with FLUXCOM and MODIS for AMSR2 than for AMSR-E even without including temperature in the model. This indicates that, in addition to the temperature dependency of R_a, other effects play an important role, which need to be considered for a more robust estimation of GPP based on VOD. These parameters likely include the choice of training data as demonstrated by the variability in mean annual GPP during the uncertainty analysis.

Another simplification is that our model assumes similar temporal dynamics of above- and belowground biomass, which allows expressing biomass as function of VOD. The ratio of above- and belowground growth, however, may vary between years in response to environmental stresses like droughts, as shown by Doughty et al. (2015) for forest plots in the Amazon basin. Depending on the strength of this effect, mismatches in above- and belowground dynamics can potentially lead to differences between the VOD-based upscaling of GPP and GPP retrieved from optical data.

In general, differences and temporal shifts between GPP derived from microwave and optical data can point towards additional terms of carbon loss or storage that were not considered in the simplified model formulation. A study conducted by Würth et al. (2005) demonstrated for a semi-deciduous tropical forest how seasonal variations in the concentration of non-structural carbohydrates can support temporal shifts between carbon assimilation and vegetation growth. Therefore, differences between source- and sink-driven GPP can potentially give further insight into large-scale patterns of carbon partitioning or allocation.

7. Conclusion

We have proposed a model for estimating GPP globally based on single frequency microwave satellite VOD. The approach uses VOD as proxy for aboveground living biomass and describes the relationship between VOD and GPP through a differential equation, which connects VOD and its derivative. Using temporal changes in consecutive VOD observations (ΔVOD) as approximation for the derivative, we implemented the model using Generalized Additive Models. The proposed model is driven by VOD-based observations of vegetation biomass, and thus presents a sink-driven approach. Our results show that the model performs well in temporal extrapolation but requires further input variables like the grid cell median VOD for spatial extrapolation of the VOD-GPP relationship. We have attributed this behavior to varying proportions of structural components captured by the VOD signal, which contribute less to the GPP estimation and may be reduced by including median VOD. Our approach tends to overestimate GPP with respect to FLUXCOM and MODIS GPP, which is probably caused by the lack of temperature dependency of autotrophic respiration in the current model formulation. Overall, our results demonstrate the global applicability of the model and highlight the potential use of microwave VOD for providing GPP estimates that are complementary to source-driven approaches based on optical remote sensing data.

8. Acknowledgements

The study is performed as part of the EOWAVE project funded by the TU Wien Wissenschaftspreis 2015 awarded to Wouter Dorigo by the Vienna University of Technology (`http://climers.geo.tuwien.ac.at/eowave/`) and the STR3S project (SR/02/329) funded by the Belgian Science Policy Office (BELSPO) as part of the STEREO III program. Diego G. Miralles acknowledges support from the European Research Council 25 (ERC) under grant agreement no. 715254 (DRY–2–DRY). This work used eddy covariance data acquired and shared by the FLUXNET community, including these networks: AmeriFlux, AfriFlux, AsiaFlux, CarboAfrica, CarboEuropeIP, CarboItaly, CarboMont, ChinaFlux, Fluxnet-Canada, GreenGrass, ICOS, KoFlux, LBA, NECC, OzFlux-TERN, TCOS-Siberia, and USCCC. The FLUXNET eddy covariance data processing and harmonization was carried out by the ICOS Ecosystem Thematic Center, AmeriFlux Management Project and Fluxdata project of FLUXNET, with the support of CDIAC, and the OzFlux, ChinaFlux and AsiaFlux offices.

References

Akaike, H., 1974. A new look at the statistical model identification. IEEE transactions on automatic control 19, 716–723.

Alemohammad, S.H., Fang, B., Konings, A.G., Aires, F., Green, J.K., Kolassa, J., Gonzalez Miralles, D., Prigent, C., Gentine, P., 2017. Water, energy, and carbon with artificial neural networks (wecann): a statistically based estimate of global surface turbulent fluxes and gross primary productivity using solar-induced fluorescence. Biogeosciences 14, 4101–4124.

Andela, N., Liu, Y.Y., van Dijk, A.I.J.M., de Jeu, R.A.M., McVicar, T.R., 2013. Global changes in dryland vegetation dynamics (1988-2008) assessed by satellite remote sensing: comparing a new passive microwave vegetation density record with reflective greenness data. Biogeosciences 10, 6657–6676. URL: http://www.biogeosciences.net/10/6657/2013/, doi:10.5194/bg-10-6657-2013.

Atkin, O.K., Bruhn, D., Hurry, V.M., Tjoelker, M.G., 2005. Evans review no. 2: The hot and the cold: unravelling the variable response of plant respiration to temperature. Functional Plant Biology 32, 87–105.

Atkin, O.K., Tjoelker, M.G., 2003. Thermal acclimation and the dynamic response of plant respiration to temperature. Trends in plant science 8, 343–351.

Bais, H.P., Weir, T.L., Perry, L.G., Gilroy, S., Vivanco, J.M., 2006. The role of root exudates in rhizosphere interactions with plants and other organisms. Annual Review of Plant Biology 57, 233–266. URL: http://www.annualreviews.org/doi/10.1146/annurev.arplant.57.032905.105159, doi:10.1146/annurev.arplant.57.032905.105159.

Baldocchi, D.D., 2003. Assessing the eddy covariance technique for evaluating carbon dioxide exchange rates of ecosystems: past, present and future. Global Change Biology 9, 479–492. URL: https://onlinelibrary.wiley.com/doi/abs/10.1046/j.1365-2486.2003.00629.x, doi:10.1046/j.1365-2486.2003.00629.x.

Barnard, D.M., Meinzer, F.C., Lachenbruch, B., McCulloh, K.A., Johnson, D.M., Woodruff, D.R., 2011. Climate-related trends in sapwood biophysical properties in two conifers: avoidance of hydraulic dysfunction through coordinated adjustments in xylem efficiency, safety and capacitance. Plant, Cell & Environment 34, 643–654.

Beck, H.E., Van Dijk, A.I., Levizzani, V., Schellekens, J., Gonzalez Miralles, D., Martens, B., De Roo, A., 2017. Mswep: 3-hourly 0.25 global gridded precipitation (1979-2015) by merging gauge, satellite, and reanalysis data. Hydrology and Earth System Sciences 21, 589–615.

Beer, C., Reichstein, M., Tomelleri, E., Ciais, P., Jung, M., Carvalhais, N., Rödenbeck, C., Arain, M.A., Baldocchi, D., Bonan, G.B., Bondeau, A., Cescatti, A., Lasslop, G., Lindroth, A., Lomas, M., Luyssaert, S., Margolis, H., Oleson, K.W., Roupsard, O., Veenendaal, E., Viovy, N., Williams, C., Woodward, F.I., Papale, D., 2010. Terrestrial Gross Carbon Dioxide Uptake: Global Distribution and Covariation with Climate. Science 329, 834–838. URL: http://science.sciencemag.org/content/329/5993/834, doi:10.1126/science.1184984.

Bertin, C., Yang, X., Weston, L.A., 2003. The role of root exudates and allelochemicals in the rhizosphere. Plant and Soil 256, 67–83. URL: https://link.springer.com/article/10.1023/A:1026290508166, doi:10.1023/A:1026290508166.

Bonan, G., 2015. Ecological Climatology: Concepts and Applications. URL: https://books.google.at/books/about/Ecological_Climatology.html?id=kq8kDQAAQBAJ.

Brodribb, T.J., Holbrook, N.M., 2003. Stomatal closure during leaf dehydration, correlation with other leaf physiological traits. Plant Physiology 132, 2166–2173.

Chen, B., Ge, Q., Fu, D., Yu, G., Sun, X., Wang, S., Wang, H., 2010. A data-model fusion approach for upscaling gross ecosystem productivity to the landscape scale based on remote sensing and flux footprint modelling. Biogeosciences 7, 2943–2958. URL: http://www.biogeosciences.net/7/2943/2010/, doi:10.5194/bg-7-2943-2010.

Clark, D.A., Brown, S., Kicklighter, D.W., Chambers, J.Q., Thomlinson, J.R., Ni, J., 2001a. Measuring net primary production in forests: Concepts and field methods. Ecological Applications 11, 356–370. URL: http://onlinelibrary.wiley.com/doi/10.1890/1051-0761(2001)011[0356:MNPPIF]2.0.CO;2/abstract, doi:10.1890/1051-0761(2001)011[0356:MNPPIF]2.0.CO;2.

Clark, D.A., Brown, S., Kicklighter, D.W., Chambers, J.Q., Thomlinson, J.R., Ni, J., Holland, E.A., 2001b. Net Primary Production in Tropical Forests: An Evaluation and Synthesis of existing field data. Ecological Applications 11, 371–384. URL: ftp://ftp.forest.sr.unh.edu/pub/MLSmith/John20R/Backup/NPP,carbon20pub/i1051-0761-011-02-0371.pdf.

D'Agostino, R., Pearson, E.S., 1973. Tests for departure from normality. Empirical results for the distributions of b2 and $\sqrt{b1}$. Biometrika 60, 613–622. URL: http://biomet.oxfordjournals.org/content/60/3/613, doi:10.1093/biomet/60.3.613.

D'Agostino, R.B., 1971. An omnibus test of normality for moderate and large size samples. Biometrika 58, 341–348. URL: http://biomet.oxfordjournals.org/content/58/2/341, doi:10.1093/biomet/58.2.341.

Damm, A., Guanter, L., Paul-Limoges, E., van der Tol, C., Hueni, A., Buchmann, N., Eugster, W., Ammann, C., Schaepman, M.E., 2015. Far-red sun-induced chlorophyll fluorescence shows ecosystem-specific relationships to gross primary production: An assessment based on observational and modeling approaches. Remote Sensing of Environment 166, 91–105. URL: http://www.sciencedirect.com/science/article/pii/S0034425715300341, doi:10.1016/j.rse.2015.06.004.

Damour, G., Simonneau, T., Cochard, H., Urban, L., 2010. An overview of models of stomatal conductance at the leaf level. Plant, Cell & Environment 33, 1419–1438. URL: https://onlinelibrary.wiley.com/doi/abs/10.1111/j.1365-3040.2010.02181.x, doi:10.1111/j.1365-3040.2010.02181.x.

Dee, D.P., Uppala, S.M., Simmons, A.J., Berrisford, P., Poli, P., Kobayashi, S., Andrae, U., Balmaseda, M.A., Balsamo, G., Bauer, P., Bechtold, P., Beljaars, A.C.M., van de Berg, L., Bidlot, J., Bormann, N., Delsol, C., Dragani, R., Fuentes, M., Geer, A.J., Haimberger, L., Healy, S.B., Hersbach, H., Hólm, E.V., Isaksen, L., Kållberg, P., Köhler, M., Matricardi, M., McNally, A.P., Monge-Sanz, B.M., Morcrette, J.J., Park, B.K., Peubey, C., de Rosnay, P., Tavolato, C., Thépaut, J.N., Vitart, F., 2011. The ERA-Interim reanalysis: configuration and performance of the data assimilation system. Quarterly Journal of the Royal Meteorological Society 137, 553–597. URL: http://onlinelibrary.wiley.com/doi/10.1002/qj.828/abstract, doi:10.1002/qj.828.

Doughty, C.E., Metcalfe, D.B., Girardin, C.A.J., Amézquita, F.F., Cabrera, D.G., Huasco, W.H., Silva-Espejo, J.E., Araujo-Murakami, A., da Costa, M.C., Rocha, W., Feldpausch, T.R., Mendoza, A.L.M., da Costa, A.C.L., Meir, P., Phillips, O.L., Malhi, Y., 2015. Drought impact on forest carbon dynamics and fluxes in Amazonia. Nature 519, 78–82. URL: http://www.nature.com/doifinder/10.1038/nature14213, doi:10.1038/nature14213.

Du, J., Kimball, J.S., Jones, L.A., Kim, Y., Glassy, J., Watts, J.D., 2017. A global satellite environmental data record derived from AMSR-E and AMSR2 microwave Earth observations. Earth System Science Data 9, 791–808. URL: https://www.earth-syst-sci-data.net/9/791/2017/, doi:10.5194/essd-9-791-2017.

Fatichi, S., Leuzinger, S., Körner, C., 2014. Moving beyond photosynthesis:

from carbon source to sink-driven vegetation modeling. New Phytologist 201, 1086–1095.

Forkel, M., Dorigo, W., Lasslop, G., Teubner, I., Chuvieco, E., Thonicke, K., 2017. A data-driven approach to identify controls on global fire activity from satellite and climate observations (SOFIA V1). Geoscientific Model Development 10, 4443–4476. URL: https://www.geosci-model-dev.net/10/4443/2017/, doi:10.5194/gmd-10-4443-2017.

Frankenberg, C., Fisher, J.B., Worden, J., Badgley, G., Saatchi, S.S., Lee, J.E., Toon, G.C., Butz, A., Jung, M., Kuze, A., Yokota, T., 2011. New global observations of the terrestrial carbon cycle from GOSAT: Patterns of plant fluorescence with gross primary productivity. Geophysical Research Letters 38. URL: https://agupubs.onlinelibrary.wiley.com/doi/abs/10.1029/2011GL048738, doi:10.1029/2011GL048738.

Frankenberg, C., O'Dell, C., Berry, J., Guanter, L., Joiner, J., Köhler, P., Pollock, R., Taylor, T.E., 2014. Prospects for chlorophyll fluorescence remote sensing from the Orbiting Carbon Observatory-2. Remote Sensing of Environment 147, 1–12. URL: http://linkinghub.elsevier.com/retrieve/pii/S0034425714000522, doi:10.1016/j.rse.2014.02.007.

Gifford, R.M., 2003. Plant respiration in productivity models: conceptualisation, representation and issues for global terrestrial carbon-cycle research. Functional Plant Biology 30, 171–186.

Gilabert, M.A., Sánchez-Ruiz, S., Moreno, l., 2017. Annual Gross Primary Production from Vegetation Indices: A Theoretically Sound Approach. Remote Sensing 9, 193. URL: http://www.mdpi.com/2072-4292/9/3/193, doi:10.3390/rs9030193.

Girardin, C.a.J., Malhi, Y., Aragão, L.E.O.C., Mamani, M., Huaraca Huasco, W., Durand, L., Feeley, K.J., Rapp, J., Silva-Espejo, J.E., Silman, M., Salinas, N., Whittaker, R.J., 2010. Net primary productivity allocation and cycling of carbon along a tropical forest elevational transect in the Peruvian Andes. Global Change Biology 16, 3176–3192. URL: http://onlinelibrary.wiley.com/doi/10.1111/j.1365-2486.2010.02235.x/full, doi:10.1111/j.1365-2486.2010.02235.x.

Good, S.P., Moore, G.W., Miralles, D.G., 2017. A mesic maximum in biological water use demarcates biome sensitivity to aridity shifts. Nature ecology & evolution 1, 1883.

Gower, S.T., Krankina, O., Olson, R.J., Apps, M., Linder, S., Wang, C., 2001. Net primary production and carbon allocation patterns of boreal forest ecosystems. Ecological Applications 11, 1395–1411. URL: http://onlinelibrary.wiley.com/doi/10.1890/1051-0761(2001)011[1395:NPPACA]2.0.CO;2/full, doi:10.1890/1051-0761(2001)011[1395:NPPACA]2.0.CO;2.

Greve, P., Orlowsky, B., Mueller, B., Sheffield, J., Reichstein, M., Seneviratne, S.I., 2014. Global assessment of trends in wetting and drying over land. Nature geoscience 7, 716.

Guan, K., Berry, J.A., Zhang, Y., Joiner, J., Guanter, L., Badgley, G., Lobell, D.B., 2016. Improving the monitoring of crop productivity using spaceborne solar-induced fluorescence. Global Change Biology 22, 716–726. URL: https://onlinelibrary.wiley.com/doi/abs/10.1111/gcb.13136, doi:10.1111/gcb.13136.

Guanter, L., Zhang, Y., Jung, M., Joiner, J., Voigt, M., Berry, J.A., Frankenberg, C., Huete, A.R., Zarco-Tejada, P., Lee, J.E., Moran, M.S., Ponce-Campos, G., Beer, C., Camps-Valls, G., Buchmann, N., Gianelle, D., Klumpp, K., Cescatti, A., Baker, J.M., Griffis, T.J., 2014. Global and time-resolved monitoring of crop photosynthesis with chlorophyll fluorescence. Proceedings of the National Academy of Sciences 111, E1327–E1333. URL: http://www.pnas.org/content/111/14/E1327, doi:10.1073/pnas.1320008111.

Guenther, A., 2002. The contribution of reactive carbon emissions from vegetation to the carbon balance of terrestrial ecosystems. Chemosphere 49, 837–844. URL: http://www.sciencedirect.com/science/article/pii/S0045653502003843, doi:10.1016/S0045-6535(02)00384-3.

Hastie, T., Tibshirani, R., 1987. Generalized Additive Models: Some Applications. Journal of the American Statistical Association 82, 371–386. URL: https://www.tandfonline.com/doi/abs/10.1080/01621459.1987.10478440, doi:10.1080/01621459.1987.10478440.

Hastie, T., Tibshirani, R., 1990. Generalized additive models. Chapman & Hall/CRC, Boca Raton, Fla.

Huffman, G.J., Adler, R.F., Morrissey, M.M., Bolvin, D.T., Curtis, S., Joyce, R., McGavock, B., Susskind, J., 2001. Global Precipitation at One-Degree Daily Resolution from Multisatellite Observations. Journal of Hydrometeorology 2, 36–50. URL: http://journals.ametsoc.org/doi/full/10.1175/1525-7541(2001)0023C00363AGPAODD3E2.0.CO3B2, doi:10.1175/1525-7541(2001)002<0036:GPAODD>2.0.CO;2.

Jackson, T.J., Schmugge, T.J., 1991. Vegetation effects on the microwave emission of soils. Remote Sensing of Environment 36, 203–212. URL: http://www.sciencedirect.com/science/article/pii/003442579190057D, doi:10.1016/0034-4257(91)90057-D.

Joiner, J., Guanter, L., Lindstrot, R., Voigt, M., Vasilkov, A.P., Middleton, E.M., Huemmrich, K.F., Yoshida, Y., Frankenberg, C., 2013. Global monitoring of terrestrial chlorophyll fluorescence from moderate-spectral-resolution near-infrared satellite measurements: methodology, simulations, and application to GOME-2. Atmospheric Measurement Techniques 6, 2803–2823. URL: http://www.atmos-meas-tech.net/6/2803/2013/amt-6-2803-2013.pdf.

Joiner, J., Yoshida, Y., Guanter, L., Middleton, E.M., 2016. New methods for the retrieval of chlorophyll red fluorescence from hyperspectral satellite instruments: simulations and application to GOME-2 and SCIAMACHY. Atmospheric Measurement Techniques 9, 3939–3967. URL: http://www.atmos-meas-tech.net/9/3939/2016/amt-9-3939-2016-discussion.html, doi:10.5194/amt-9-3939-2016.

Joiner, J., Yoshida, Y., Vasilkov, A.P., Schaefer, K., Jung, M., Guanter, L., Zhang, Y., Garrity, S., Middleton, E.M., Huemmrich, K.F., Gu, L., Belelli Marchesini, L., 2014. The seasonal cycle of satellite chlorophyll fluorescence observations and its relationship to vegetation phenology and ecosystem atmosphere carbon exchange. Remote Sensing of Environment 152, 375–391. URL: http://www.sciencedirect.com/science/article/pii/S0034425714002429, doi:10.1016/j.rse.2014.06.022.

Jones, D.L., Nguyen, C., Finlay, R.D., 2009. Carbon flow in the rhizosphere: carbon trading at the soil–root interface. Plant and Soil 321, 5–33. URL: http://link.springer.com/10.1007/s11104-009-9925-0, doi:10.1007/s11104-009-9925-0.

Jones, M.O., Jones, L.A., Kimball, J.S., McDonald, K.C., 2011. Satellite passive microwave remote sensing for monitoring global land surface phenology. Remote Sensing of Environment 115, 1102–1114. URL: http://www.sciencedirect.com/science/article/pii/S0034425710003615, doi:10.1016/j.rse.2010.12.015.

Jung, M., Reichstein, M., Bondeau, A., 2009. Towards global empirical upscaling of FLUXNET eddy covariance observations: validation of a model tree ensemble approach using a biosphere model. Biogeosciences 6, 2001–2013. URL: http://www.biogeosciences.net/6/2001/2009/bg-6-2001-2009.html, doi:10.5194/bg-6-2001-2009.

Jung, M., Reichstein, M., Margolis, H.A., Cescatti, A., Richardson, A.D., Arain, M.A., Arneth, A., Bernhofer, C., Bonal, D., Chen, J., Gianelle, D., Gobron, N., Kiely, G., Kutsch, W., Lasslop, G., Law, B.E., Lindroth, A., Merbold, L., Montagnani, L., Moors, E.J., Papale, D., Sottocornola, M., Vaccari, F., Williams, C., 2011. Global patterns of land-atmosphere fluxes of carbon dioxide, latent heat, and sensible heat derived from eddy covariance, satellite, and meteorological observations. Journal of Geophysical Research 116, G00J07. URL: http://doi.wiley.com/10.1029/2010JG001566, doi:10.1029/2010JG001566.

Kesselmeier, J., Ciccioli, P., Kuhn, U., Stefani, P., Biesenthal, T., Rottenberger, S., Wolf, A., Vitullo, M., Valentini, R., Nobre, A., Kabat, P., Andreae, M.O., 2002. Volatile organic compound emissions in relation to plant carbon fixation and the terrestrial carbon budget. Global Biogeochemical Cycles 16. URL: http://onlinelibrary.wiley.com/doi/10.1029/2001GB001813/full, doi:10.1029/2001GB001813.

Klein, T., 2014. The variability of stomatal sensitivity to leaf water potential across tree species indicates a continuum between isohydric and anisohydric behaviours. Functional Ecology 28, 1313–1320.

Konings, A.G., Gentine, P., 2016. Global variations in ecosystem-scale isohydricity. Global Change Biology 23, 891–905. URL: http://doi.wiley.com/10.1111/gcb.13389, doi:10.1111/gcb.13389.

Konings, A.G., Williams, A.P., Gentine, P., 2017a. Sensitivity of grassland productivity to aridity controlled by stomatal and xylem regulation. Nature Geoscience URL: http://www.nature.com/doifinder/10.1038/ngeo2903, doi:10.1038/ngeo2903.

Konings, A.G., Yu, Y., Xu, L., Yang, Y., Schimel, D.S., Saatchi, S.S., 2017b. Active microwave observations of diurnal and seasonal variations of canopy water content across the humid African tropical forests. Geophysical Research Letters 44, 2290–2299. URL: https://agupubs.onlinelibrary.wiley.com/doi/abs/10.1002/2016GL072388, doi:10.1002/2016GL072388.

Körner, C., 2015. Paradigm shift in plant growth control. Current opinion in plant biology 25, 107–114.

Lasslop, G., Reichstein, M., Papale, D., Richardson, A.D., Arneth, A., Barr, A., Stoy, P., Wohlfahrt, G., 2010. Separation of net ecosystem exchange into assimilation and respiration using a light response curve approach: critical issues and global evaluation. Global Change Biology

16, 187–208. URL: http://onlinelibrary.wiley.com/doi/10.1111/j.1365-2486.2009.02041.x/abstract, doi:10.1111/j.1365-2486.2009.02041.x.

Lavigne, M., Ryan, M., 1997. Growth and maintenance respiration rates of aspen, black spruce and jack pine stems at northern and southern BOREAS sites. Tree Physiology 17, 543–551.

Leuzinger, S., Manusch, C., Bugmann, H., Wolf, A., 2013. A sink-limited growth model improves biomass estimation along boreal and alpine tree lines. Global Ecology and Biogeography 22, 924–932.

Li, L., Njoku, E.G., Im, E., Chang, P.S., Germain, K.S., 2004. A preliminary survey of radio-frequency interference over the U.S. in Aqua AMSR-E data. IEEE Transactions on Geoscience and Remote Sensing 42, 380–390. doi:10.1109/TGRS.2003.817195.

Litton, C.M., Raich, J.W., Ryan, M.G., 2007. Carbon allocation in forest ecosystems. Global Change Biology 13, 2089–2109. URL: https://onlinelibrary.wiley.com/doi/abs/10.1111/j.1365-2486.2007.01420.x, doi:10.1111/j.1365-2486.2007.01420.x.

Liu, Y.Y., van Dijk, A.I.J.M., de Jeu, R.A.M., Canadell, J.G., McCabe, M.F., Evans, J.P., Wang, G., 2015. Recent reversal in loss of global terrestrial biomass. Nature Climate Change 5, 470–474. URL: http://www.nature.com/doifinder/10.1038/nclimate2581, doi:10.1038/nclimate2581.

Liu, Y.Y., van Dijk, A.I.J.M., McCabe, M.F., Evans, J.P., de Jeu, R.A.M., 2013a. Global vegetation biomass change (1988-2008) and attribution to environmental and human drivers: Global vegetation biomass change. Global Ecology and Biogeography 22, 692–705. URL: http://doi.wiley.com/10.1111/geb.12024, doi:10.1111/geb.12024.

Liu, Y.Y., Evans, J.P., McCabe, M.F., de Jeu, R.A.M., van Dijk, A.I.J.M., Dolman, A.J., Saizen, I., 2013b. Changing Climate and Overgrazing Are Decimating Mongolian Steppes. PLoS ONE 8, e57599. URL: http://dx.plos.org/10.1371/journal.pone.0057599, doi:10.1371/journal.pone.0057599.

Liu, Y.Y., Jeu, D., M, R.A., McCabe, M.F., Evans, J.P., Dijk, V., M, A.I.J., 2011. Global long-term passive microwave satellite-based retrievals of vegetation optical depth. Geophysical Research Letters 38. URL: http://onlinelibrary.wiley.com/doi/10.1029/2011GL048684/abstract, doi:10.1029/2011GL048684.

Luyssaert, S., Inglima, I., Jung, M., Richardson, A.D., Reichstein, M., Papale, D., Piao, S.L., Schulze, E.D., Wingate, L., Matteucci, G., Aragao, L., Aubinet, M., Beer, C., Bernhofer, C., Black, K.G., Bonal, D., Bonnefond, J.M., Chambers, J., Ciais, P., Cook, B., Davis, K.J., Dolman, A.J., Gielen, B., Goulden, M., Grace, J., Granier, A., Grelle, A., Griffis, T., Grünwald, T., Guidolotti, G., Hanson, P.J., Harding, R., Hollinger, D.Y., Hutyra, L.R., Kolari, P., Kruijt, B., Kutsch, W., Lagergren, F., Laurila, T., Law, B.E., Le Maire, G., Lindroth, A., Loustau, D., Malhi, Y., Mateus, J., Migliavacca, M., Misson, L., Montagnani, L., Moncrieff, J., Moors, E., Munger, J.W., Nikinmaa, E., Ollinger, S.V., Pita, G., Rebmann, C., Roupsard, O., Saigusa, N., Sanz, M.J., Seufert, G., Sierra, C., Smith, M.L., Tang, J., Valentini, R., Vesala, T., Janssens, I.A., 2007. CO2 balance of boreal, temperate, and tropical forests derived from a global database. Global Change Biology 13, 2509–2537. URL: http://onlinelibrary.wiley.com/doi/10.1111/j.1365-2486.2007.01439.x/abstract, doi:10.1111/j.1365-2486.2007.01439.x.

Marle, M.J.E.v., Werf, G.R.v.d., Jeu, R.A.M.d., Liu, Y.Y., 2016. Annual South American forest loss estimates based on passive microwave remote sensing (1990-2010). Biogeosciences 13, 609–624. URL: http://www.biogeosciences.net/13/609/2016/bg-13-609-2016-relations.html, doi:10.5194/bg-13-609-2016.

Martens, B., Gonzalez Miralles, D., Lievens, H., Van Der Schalie, R., De Jeu, R.A., Fernández-Prieto, D., Beck, H.E., Dorigo, W., Verhoest, N., 2017. Gleam v3: Satellite-based land evaporation and root-zone soil moisture. Geoscientific Model Development 10, 1903–1925.

Meesters, A.G.C.A., Jeu, R.A.M.D., Owe, M., 2005. Analytical derivation of the vegetation optical depth from the microwave polarization difference index. IEEE Geoscience and Remote Sensing Letters 2, 121–123. URL: http://ieeexplore.ieee.org/articleDetails.jsp?arnumber=1420287, doi:10.1109/LGRS.2005.843983.

Melzer, T., 2013. Vegetation Modelling in WARP 6.0, in: Understanding the past, observing the present and protecting the future Vienna 2013, Vienna, Austria.

Miralles, D., Holmes, T., De Jeu, R., Gash, J., Meesters, A., Dolman, A., et al., 2011. Global land-surface evaporation estimated from satellite-based observations .

Mo, T., Choudhury, B.J., Schmugge, T.J., Wang, J.R., Jackson, T.J., 1982. A model for microwave emission from vegetation-covered fields. Journal of Geophysical Research: Oceans 87, 11229–11237. URL: http://onlinelibrary.wiley.com/doi/10.1029/JC087iC13p11229/full, doi:10.1029/JC087iC13p11229.

Momen, M., Wood, J.D., Novick, K.A., Pangle, R., Pockman, W.T., McDowell, N.G., Konings, A.G., 2017. Interacting Effects of Leaf Water Potential and Biomass on Vegetation Optical Depth. Journal of Geophysical Research: Biogeosciences 122, 3031–3046. URL: https://agupubs.onlinelibrary.wiley.com/doi/abs/10.1002/2017JG004145, doi:10.1002/2017JG004145.

Monteith, J.L., 1972. Solar Radiation and Productivity in Tropical Ecosystems. Journal of Applied Ecology 9, 747–766. URL: http://www.jstor.org/stable/2401901, doi:10.2307/2401901.

Njoku, E.G., Ashcroft, P., Chan, T.K., Li, L., 2005. Global survey and statistics of radio-frequency interference in AMSR-E land observations. IEEE Transactions on Geoscience and Remote Sensing 43, 938–947. doi:10.1109/TGRS.2004.837507.

Odum, E.P., 1959. Fundamentals of ecology. WB Saunders company.

Paulik, C., Hahn, S., Mistelbauer, T., 2015. Pytesmo: V0.3.0. URL: https://zenodo.org/record/596422, doi:10.5281/zenodo.596422.

Reichstein, M., Falge, E., Baldocchi, D., Papale, D., Aubinet, M., Berbigier, P., Bernhofer, C., Buchmann, N., Gilmanov, T., Granier, A., Grünwald, T., Havránková, K., Ilvesniemi, H., Janous, D., Knohl, A., Laurila, T., Lohila, A., Loustau, D., Matteucci, G., Meyers, T., Miglietta, F., Ourcival, J.M., Pumpanen, J., Rambal, S., Rotenberg, E., Sanz, M., Tenhunen, J., Seufert, G., Vaccari, F., Vesala, T., Yakir, D., Valentini, R., 2005. On the separation of net ecosystem exchange into assimilation and ecosystem respiration: review and improved algorithm. Global Change Biology 11, 1424–1439. URL: http://onlinelibrary.wiley.com/doi/10.1111/j.1365-2486.2005.001002.x/abstract, doi:10.1111/j.1365-2486.2005.001002.x.

Rodríguez-Fernández, N.J., Mialon, A., Mermoz, S., Bouvet, A., Richaume, P., Al Bitar, A., Al-Yaari, A., Brandt, M., Kaminski, T., Le Toan, T., Kerr, Y.H., Wigneron, J.P., 2018. The high sensitivity of SMOS L-Band vegetation optical depth to biomass. Biogeosciences Discussions , 1–20URL: https://www.biogeosciences-discuss.net/bg-2018-49/, doi:10.5194/bg-2018-49.

Running, S., Mu, Q., 2015. MOD17a2h MODIS/Terra Gross Primary Productivity 8-Day L4 Global 500m SIN Grid V006. doi:10.5067/MODIS/MOD17A2H.006.

Running, S.W., 1976. Environmental control of leaf water conductance in conifers. Canadian Journal of Forest Research URL: http://www.nrcresearchpress.com/doi/abs/10.1139/x76-013#.V_d0EMmNjlI, doi:10.1139/x76-013.

Running, S.W., Nemani, R., Glassy, J.M., Thornton, P.E., 1999. MODIS daily photosynthesis (PSN) and annual net primary production (NPP) product (MOD17) Algorithm Theoretical Basis Document. URL: www.ntsg.umt.edu/modis/ATBD/ATBD_MOD17_v21.pdf.

Running, S.W., Nemani, R.R., Heinsch, F.A., Zhao, M., Reeves, M., Hashimoto, H., 2004. A Continuous Satellite-Derived Measure of Global Terrestrial Primary Production. BioScience 54, 547–560. URL: http://bioscience.oxfordjournals.org/content/54/6/547, doi:10.1641/0006-3568(2004)054[0547:ACSMOG]2.0.CO;2.

Running, S.W., Thorton, P.E., Nemani, R., Glassy, J.M., 2000. Global Terrestrial Gross and Net Primary Productivity from the Earth Observing System, in: Methods in Ecosystem Science. URL: https://books.google.at/books/about/Methods_in_Ecosystem_Science.html?id=N_pGrSntap0C.

Ryan, M.G., 1990. Growth and maintenance respiration in stems of Pinus-contorta and Piceaengelmannii. Canadian Journal of Forest Research 20, 48–57. URL: http://www.nrcresearchpress.com/doi/abs/10.1139/x90-008#.WPf7HGclHmg, doi:10.1139/x90-008.

Ryan, M.G., 1991. Effects of climate change on plant respiration. Ecological Applications 1, 157–167.

Savitzky, A., Golay, M.J., 1964. Smoothing and differentiation of data by simplified least squares procedures. Analytical chemistry 36, 1627–1639.

van der Schalie, R., de Jeu, R.A.M., Kerr, Y.H., Wigneron, J.P., Rodríguez-Fernández, N.J., Al-Yaari, A., Parinussa, R.M., Mecklenburg, S., Drusch, M., 2017. The merging of radiative transfer based surface soil moisture data from SMOS and AMSR-E. Remote Sensing of Environment 189, 180–193. URL: http://www.sciencedirect.com/science/article/pii/S0034425716304734, doi:10.1016/j.rse.2016.11.026.

Servén, D., Brummitt, C., Abedi, H., 2018. Dswah/Pygam: V0.5.4. URL: https://zenodo.org/record/1208723, doi:10.5281/zenodo.1208723.

Smith, N.G., Dukes, J.S., 2013. Plant respiration and photosynthesis in global-scale models: incorporating acclimation to temperature and co2. Global Change Biology 19, 45–63.

Teubner, I.E., Forkel, M., Jung, M., Liu, Y.Y., Miralles, D.G., Parinussa, R., van der Schalie, R., Vreugdenhil, M., Schwalm, C.R., Tramontana, G., Camps-Valls, G., Dorigo, W.A., 2018. Assessing the relationship between microwave vegetation optical depth and gross primary production. International Journal of Applied Earth Observation and Geoinformation 65, 79–91. URL: http://www.sciencedirect.com/science/article/pii/S0303243417302258, doi:10.1016/j.jag.2017.10.006.

Tian, F., Brandt, M., Liu, Y.Y., Rasmussen, K., Fensholt, R., 2017. Mapping gains and losses in woody vegetation across global tropical drylands. Global Change Biology 23, 1748–1760. URL: https://onlinelibrary.wiley.com/doi/abs/10.1111/gcb.13464, doi:10.1111/gcb.13464.

Tian, F., Brandt, M., Liu, Y.Y., Verger, A., Tagesson, T., Diouf, A.A., Rasmussen, K., Mbow, C., Wang, Y., Fensholt, R., 2016. Remote sensing of vegetation dynamics in drylands: Evaluating vegetation optical depth (VOD) using AVHRR NDVI and in situ green biomass data over West African Sahel. Remote Sensing of Environment 177, 265–276. URL: http://linkinghub.elsevier.com/retrieve/pii/S0034425716300852, doi:10.1016/j.rse.2016.02.056.

Tjoelker, M.G., Oleksyn, J., Reich, P.B., 2001. Modelling respiration of vegetation: evidence for a general temperature-dependent q10. Global Change Biology 7, 223–230.

Tramontana, G., Ichii, K., Camps-Valls, G., Tomelleri, E., Papale, D., 2015. Uncertainty analysis of gross primary production upscaling using Random Forests, remote sensing and eddy covariance data. Remote Sensing of Environment 168, 360–373. URL: http://www.sciencedirect.com/science/article/pii/S0034425715300699, doi:10.1016/j.rse.2015.07.015.

Tramontana, G., Jung, M., Schwalm, C.R., Ichii, K., Camps-Valls, G., Ráduly, B., Reichstein, M., Arain, M.A., Cescatti, A., Kiely, G., Merbold, L., Serrano-Ortiz, P., Sickert, S., Wolf, S., Papale, D., 2016. Predicting carbon dioxide and energy fluxes across global FLUXNET sites with regression algorithms. Biogeosciences 13, 4291–4313. URL: http://www.biogeosciences.net/13/4291/2016/bg-13-4291-2016-metrics.html, doi:10.5194/bg-13-4291-2016.

Vanderwel, M.C., Slot, M., Lichstein, J.W., Reich, P.B., Kattge, J., Atkin, O.K., Bloomfield, K.J., Tjoelker, M.G., Kitajima, K., 2015. Global convergence in leaf respiration from estimates of thermal acclimation across time and space. New Phytologist 207, 1026–1037.

Vreugdenhil, M., Dorigo, W.A., Wagner, W., Jeu, R.A.M.d., Hahn, S., Marle, M.J.E.v., 2016a. Analyzing the Vegetation Parameterization in the TU-Wien ASCAT Soil Moisture Retrieval. IEEE Transactions on Geoscience and Remote Sensing 54, 3513–3531. URL: http://ieeexplore.ieee.org/articleDetails.jsp?arnumber=7410033, doi:10.1109/TGRS.2016.2519842.

Vreugdenhil, M., Hahn, S., Melzer, T., Bauer-Marschallinger, B., Reimer, C., Dorigo, W.A., Wagner, W., 2016b. Assessing Vegetation Dynamics Over Mainland Australia With Metop ASCAT. IEEE Journal of Selected Topics in Applied Earth Observations and Remote Sensing PP, 1–9. doi:10.1109/JSTARS.2016.2618838.

Wagner, W., Lemoine, G., Rott, H., 1999. A Method for Estimating Soil Moisture from ERS Scatterometer and Soil Data. Remote Sensing of Environment 70, 191–207. URL: http://www.sciencedirect.com/science/article/pii/S003442579900036X, doi:10.1016/S0034-4257(99)00036-X.

Willmott, C.J., 1981. On the Validation of Models. Physical Geography 2, 184–194. URL: https://www.tandfonline.com/doi/abs/10.1080/02723646.1981.10642213, doi:10.1080/02723646.1981.10642213.

Woodhouse, I.H., 2005. Introduction to Microwave Remote Sensing. CRC Press.

Würth, M.K., Pelaez-Riedl, S., Wright, S.J., Körner, C., 2005. Non-structural carbohydrate pools in a tropical forest. Oecologia 143, 11–24.

Wythers, K.R., Reich, P.B., Bradford, J.B., 2013. Incorporating temperature-sensitive q10 and foliar respiration acclimation algorithms modifies modeled ecosystem responses to global change. Journal of Geophysical Research: Biogeosciences 118, 77–90.

Yang, F., Ichii, K., White, M.A., Hashimoto, H., Michaelis, A.R., Votava, P., Zhu, A.X., Huete, A., Running, S.W., Nemani, R.R., 2007. Developing a continental-scale measure of gross primary production by combining MODIS and AmeriFlux data through Support Vector Machine approach. Remote Sensing of Environment 110, 109–122. URL: http://www.sciencedirect.com/science/article/pii/S0034425707000831, doi:10.1016/j.rse.2007.02.016.

Zhang, Y., Guanter, L., Berry, J.A., Tol, C.v.d., Joiner, J., 2016. Can we retrieve vegetation photosynthetic capacity paramter from solar-induced fluorescence?, in: 2016 IEEE International Geoscience and Remote Sensing Symposium (IGARSS), pp. 1711–1713. doi:10.1109/IGARSS.2016.7729437.

Zhao, M., Heinsch, F.A., Nemani, R.R., Running, S.W., 2005. Improvements of the MODIS terrestrial gross and net primary production global data set. Remote Sensing of Environment 95, 164–176. URL: http://www.sciencedirect.com/science/article/pii/S0034425705000106, doi:10.1016/j.rse.2004.12.011.

List of Figures

Figure1
Click here to download high resolution image

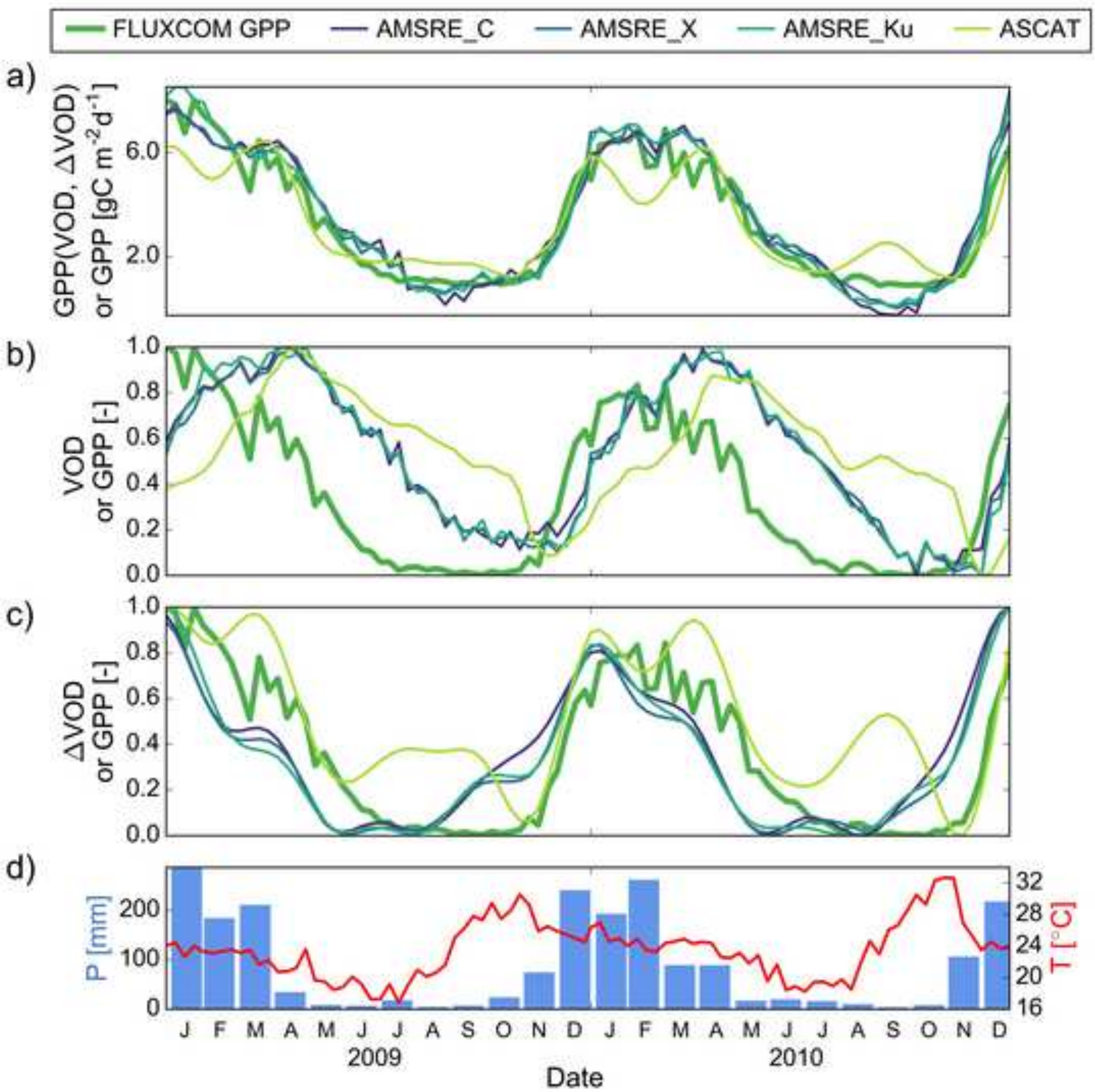

Figure2
Click here to download high resolution image

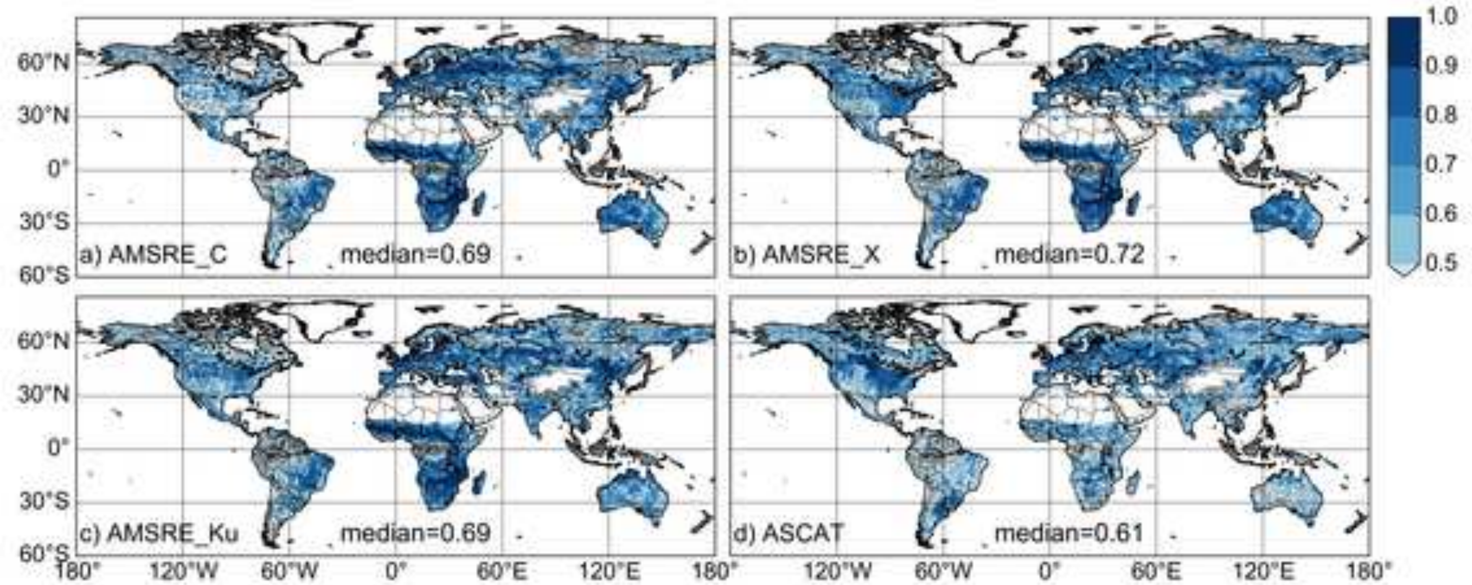

Figure3

Click here to download high resolution image

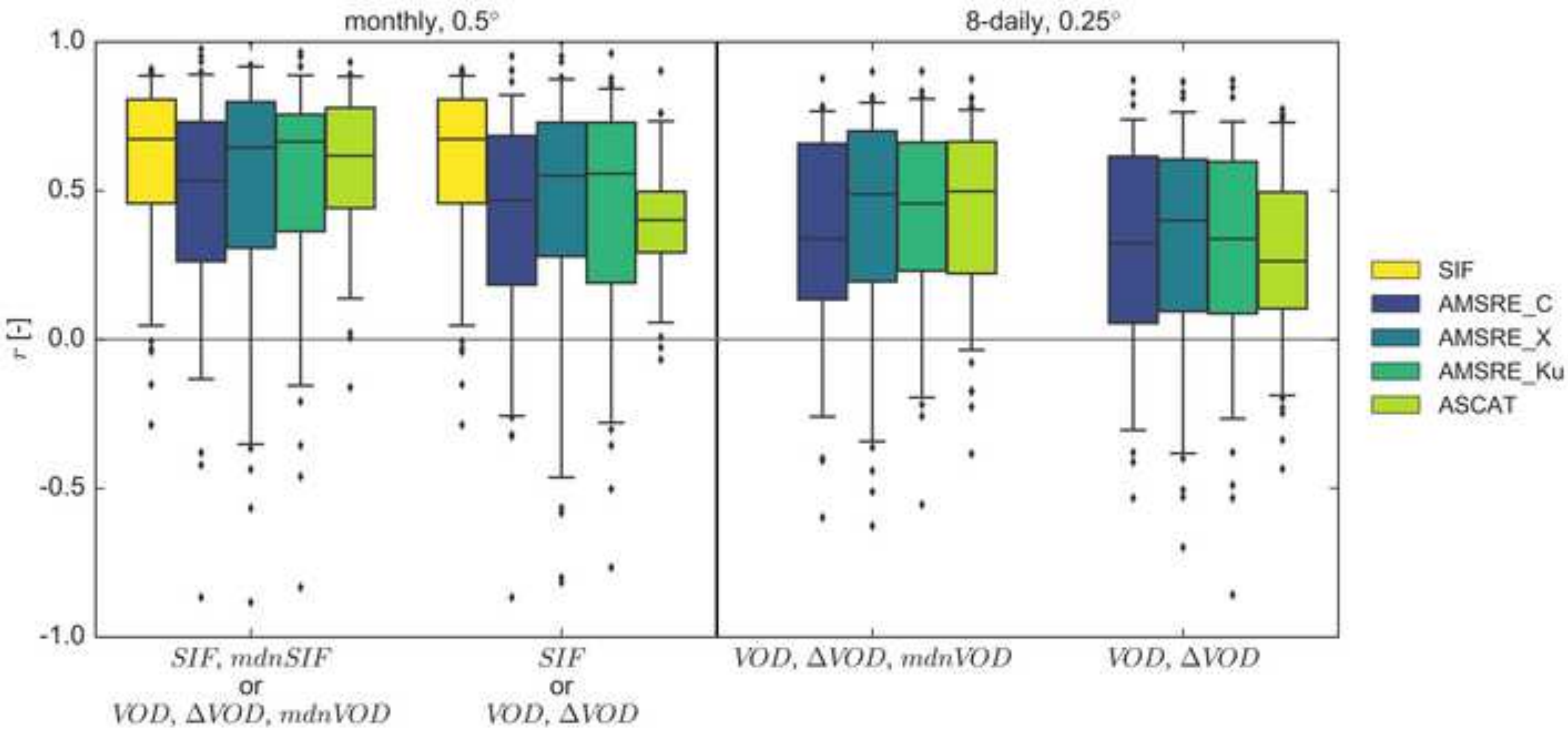

Figure4
Click here to download high resolution image

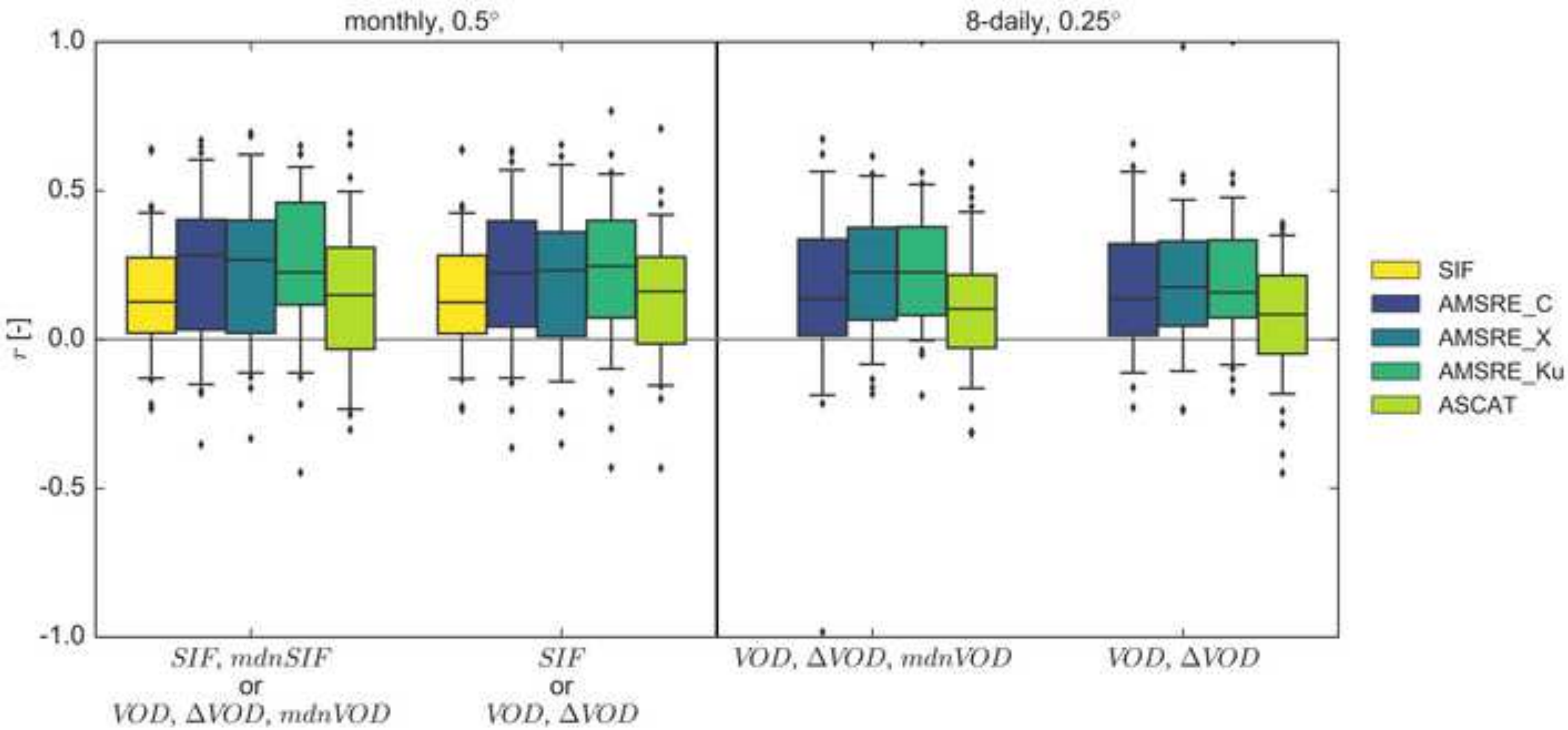

Figure5

Click here to download high resolution image

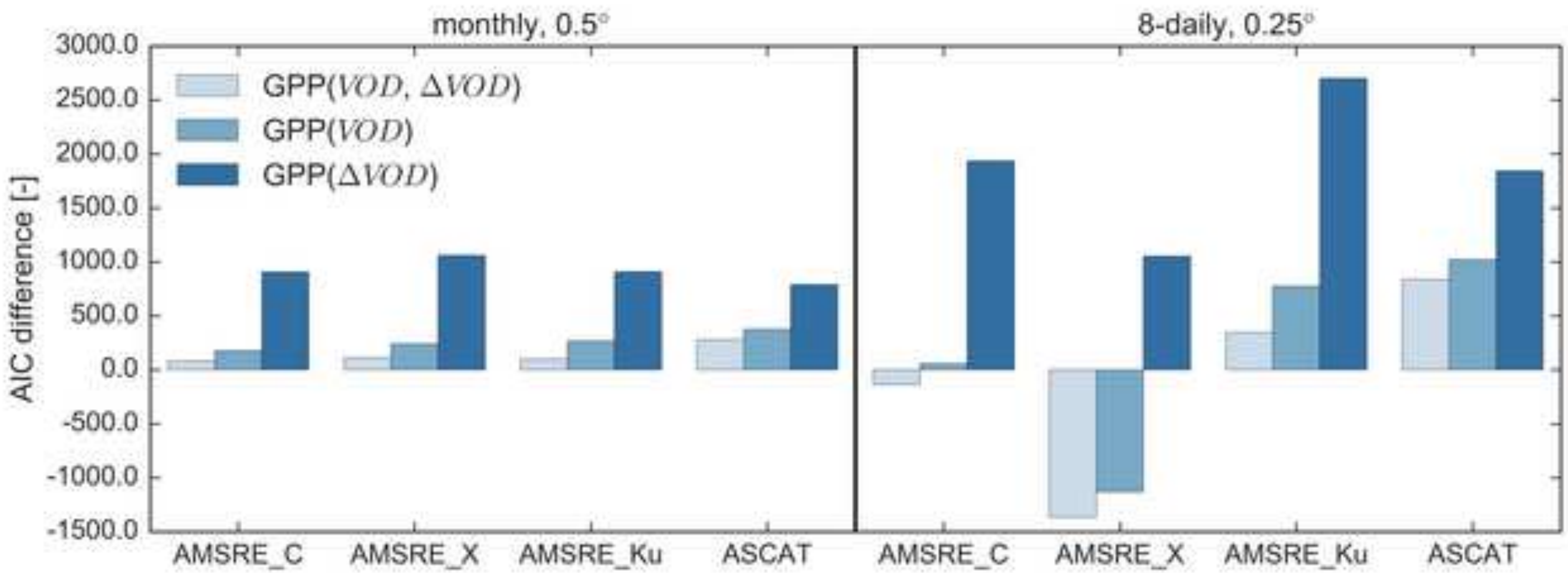

Figure6

Click here to download high resolution image

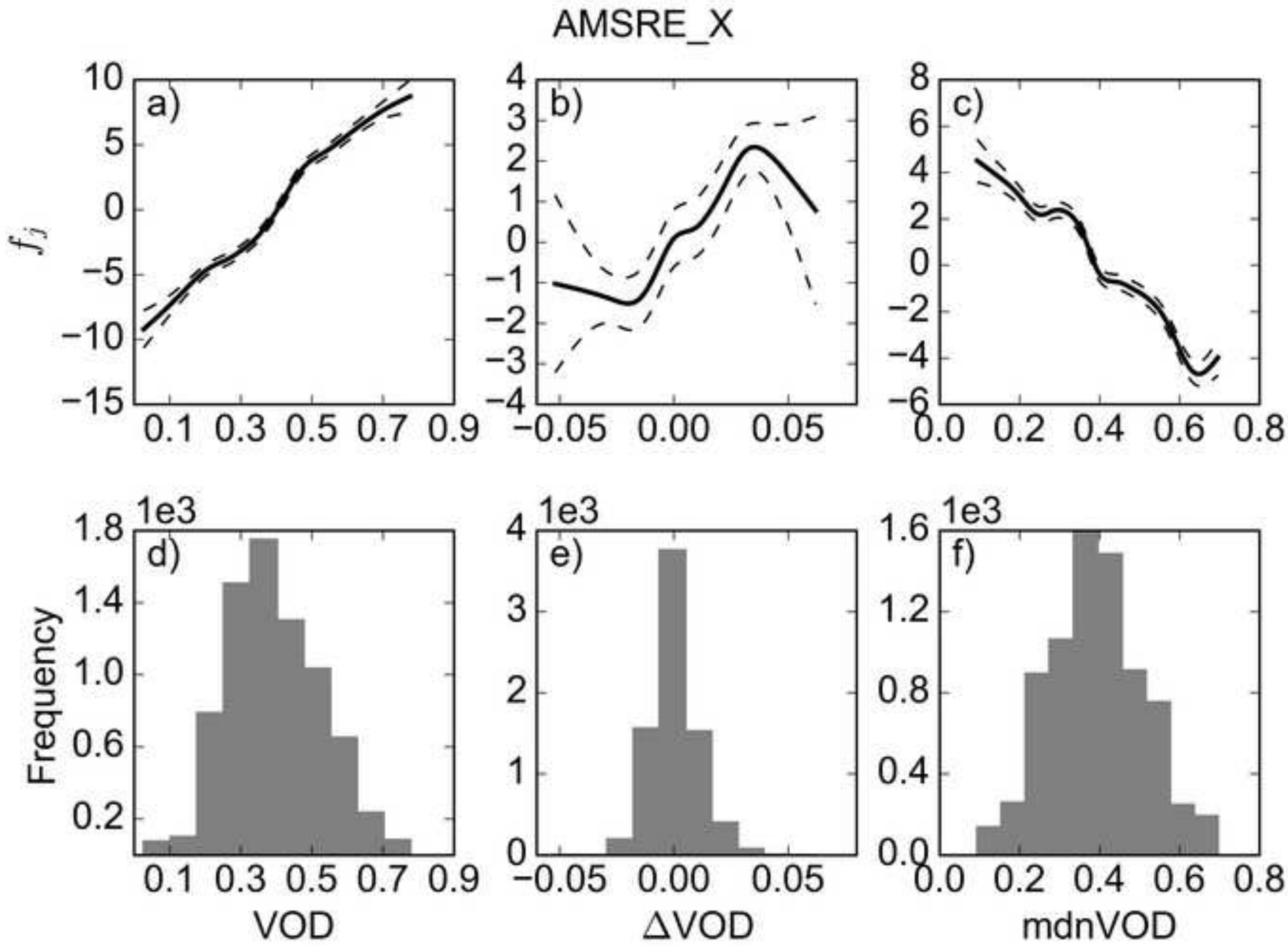

Figure7

Click here to download high resolution image

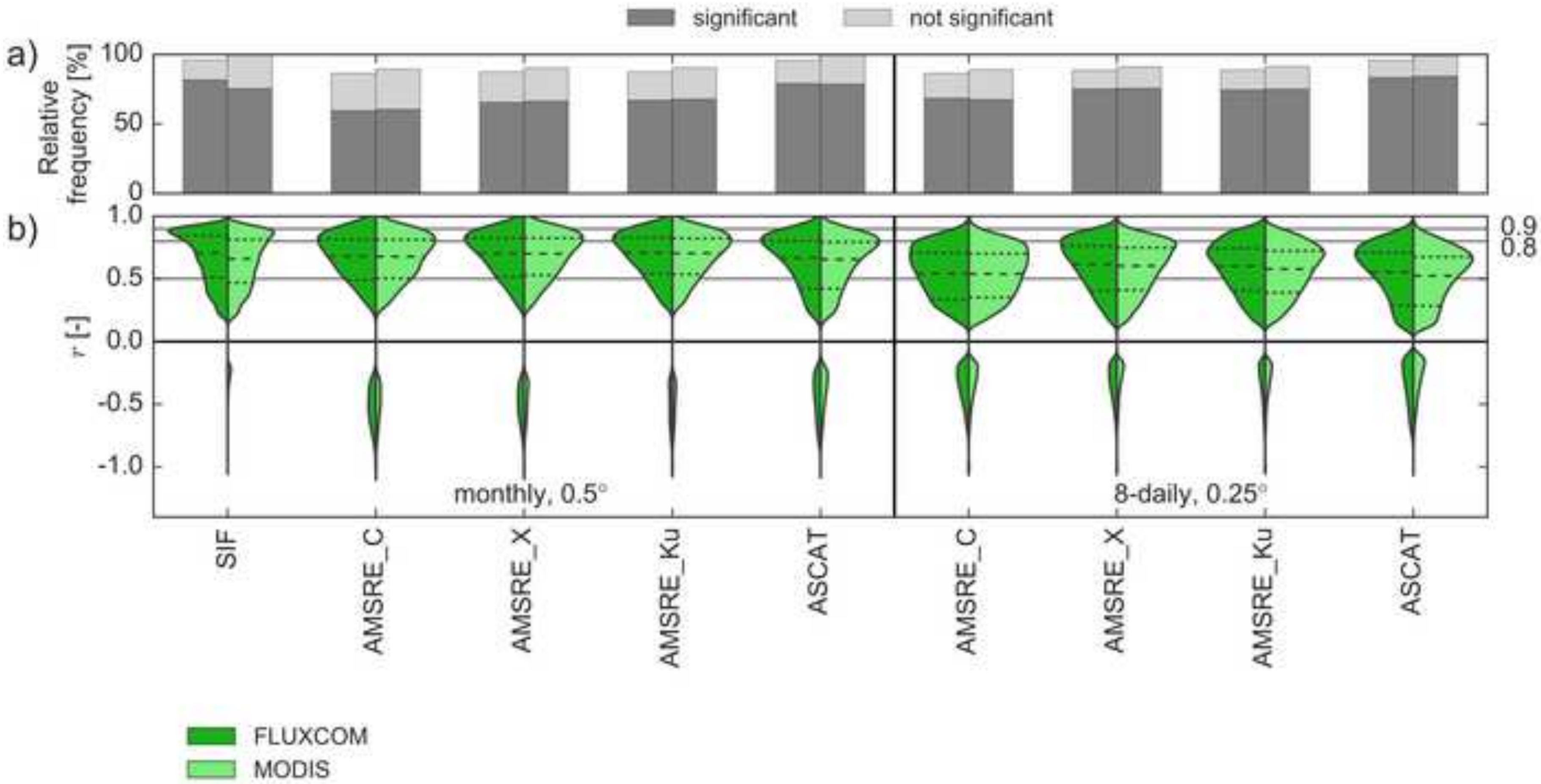

Figure8

Click here to download high resolution image

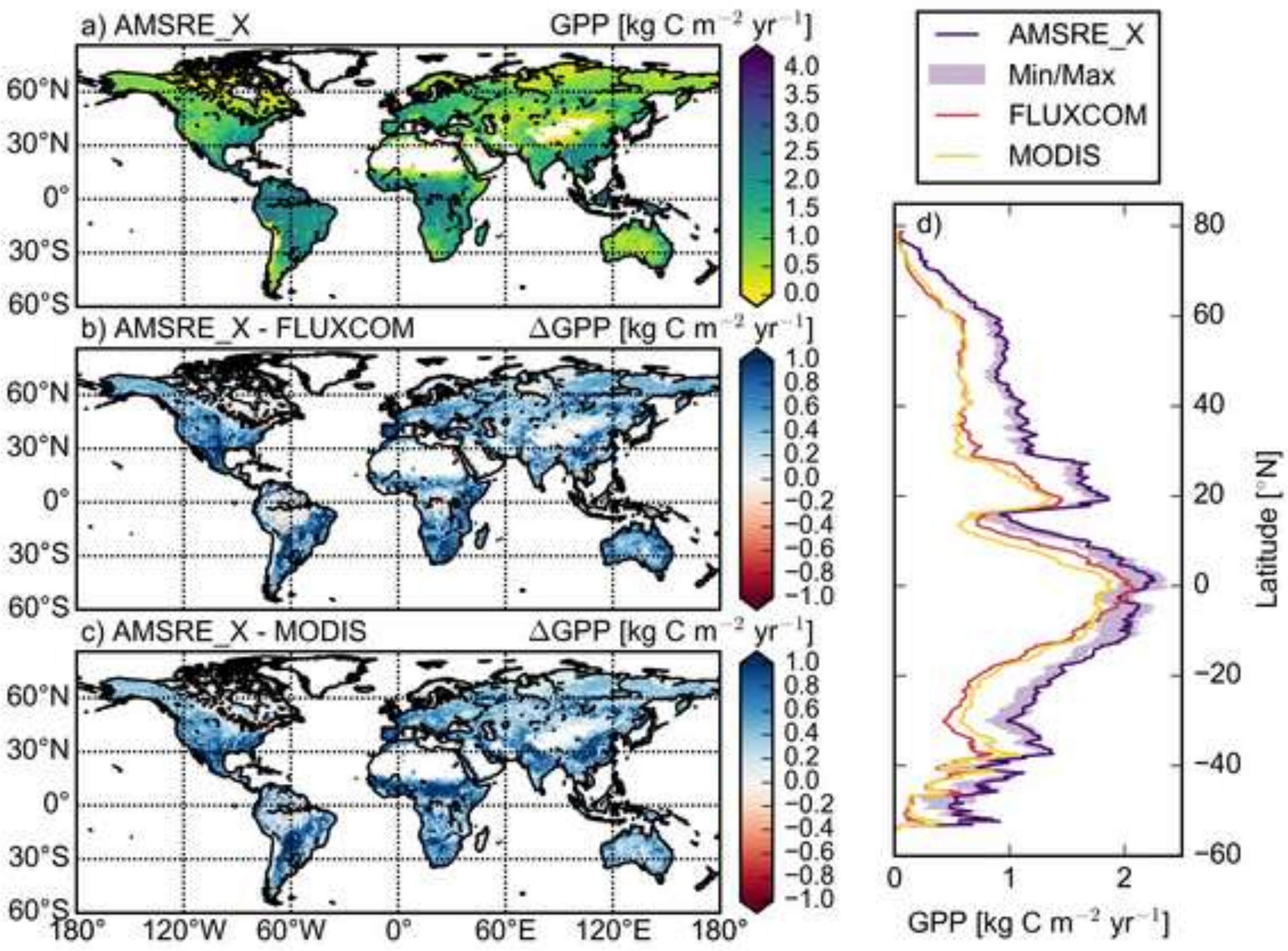

Figure9
Click here to download high resolution image